Morphological, molecular, and functional evidence for a CNS-like oral nerve ring in the sea anemone *Nematostella vectensis*

Authors

Ruohan Zhong[1], Chris W. Seidel[1], Anna M.L. Klompen[1], Matthew C. Gibson[1,*]

Affiliations

[1]Stowers Institute for Medical Research, Kansas City, MO 64110, USA

Correspondence

Matthew C. Gibson (mg2@stowers.org)

Abstract

The emergence of centralized nervous systems reflects a major inflection point in evolution, enabling animals to integrate diverse inputs and coordinate complex behaviors. Neural centralization is typically associated with Bilateria, whereas their sister group, Cnidaria (jellyfish, anemones, and corals), has long been thought to rely on diffuse nerve nets mediating simple reflexes. This view, reinforced by limited anatomical and molecular data, has left unresolved whether cnidarians can form localized centers for neural processing, a question sharpened by the growing recognition of their diverse behavioral repertoires. Here we show that the sea anemone *Nematostella vectensis* possesses an oral nerve ring composed of ganglion-like condensations, a hallmark of centralized organization. These neurons are enriched for excitatory, inhibitory, and modulatory receptors but lack sensory or ciliary markers, yielding a molecular profile most consistent with bilaterian interneurons. Genetic disruption of a conserved inhibitory receptor subunit predominantly expressed in the oral nerve ring delayed the initiation of swallowing in a novel feeding paradigm, demonstrating a potential role in behavioral regulation. Together, these findings provide converging anatomical, molecular, and functional evidence that cnidarians can assemble localized integrative centers, suggesting that key elements of neural centralization predated the cnidarian–bilaterian split.

Introduction

Animals coordinate behavior by concentrating neurons into localized integrative centers, a strategy exemplified by the bilaterian central nervous system (CNS). In contrast, cnidarians, the sister group to bilaterians, are traditionally portrayed as relying on diffuse nerve nets that mediate simple reflexes[1–4] (Fig. 1a). This dichotomy has long framed centralization as a bilaterian innovation and left unresolved whether cnidarians can assemble structures that support local integrative processing.

The diffuse nerve net paradigm has persisted for over a century, in part due to assumptions tied to cnidarians' basal phylogenetic position, the absence of macroscopic brain- or nerve cord-like structures, and a lack of molecular tools to visualize and classify neurons. *Hydra*, long the principal model for cnidarian neurobiology, further shaped this view through its diffuse, highly regenerative but lineage-specific neural organization[5,6]. Within this framework, cnidarian nerve nets were widely interpreted as morphologically and functionally simple. Still, classical anatomical studies hint that this picture might be incomplete. In 1879, Oscar and Richard Hertwig described a high density of neural elements arranged in crisscross and radial patterns in the oral disc of the parasitic anemone *Calliactis*[7]. In 1963, Elaine Robson illustrated radial oral nerve tracts in the swimming anemone *Stomphia* and proposed that they mediate coordination between the oral disc and the mesenteries[8]. In 1982, Kinnamon and Westfall identified interneuron-like cells at hypostome–tentacle junctions in *Hydra littoralis*, which they referred to as "primitive ganglia"[9]. These findings raise the possibility of localized neural organization within cnidarian nerve nets, although their cellular identities, developmental origins, and functional roles remain unknown.

Modern behavioral work strengthens this perspective by revealing functional specialization across cnidarian lineages. *Clytia hemisphaerica* relies on spatially organized subnetworks to coordinate food handling[10]; *Hydra vulgaris* displays satiety-dependent behaviors mediated by enteric- and CNS-like neuronal subpopulations[11]; the box jellyfish *Tripedalia cystophora* can modify obstacle avoidance through operant conditioning[12]; and the sea anemone *Nematostella vectensis* exhibits circadian

locomotion and associative learning[13,14]. Together, these findings indicate that cnidarian nerve nets support more structured and context-dependent processing than is captured by the classical diffuse nerve net paradigm.

Nematostella vectensis offers an ideal system to revisit these assumptions with modern tools. It combines a tractable life cycle[15,16], a well-annotated genome[17–19], and an expanding molecular toolkit[20–22]. Unlike bilaterian invertebrates such as *Drosophila* or *C. elegans*, which have undergone extensive gene loss, *Nematostella* retains a broad ancestral eumetazoan gene repertoire more comparable to vertebrates, including synaptic machinery, neurotransmitter pathways, and developmental regulators[23–30]. Despite its compact genome (269.4 Mb; ~19,200 protein-coding genes, similar to humans), our analysis of the current RefSeq assembly reveals an unexpectedly broad diversification of neurotransmitter receptor families, including glutamate, γ-aminobutyric acid (GABA), acetylcholine, monoamine, and neuropeptide receptors, well beyond the two previously characterized types[31,32] and far exceeding the diversity seen in many bilaterians (Supplementary Table 2). In contrast, receptor numbers for other signaling pathways such as BMP[33], Wnt[34], and Hedgehog[35] are comparable to or below human levels, suggesting that this diversification is specific to neural communication genes. Developmentally, *Nematostella* exhibits bilateral patterning of tentacles, musculature, and Hox/BMP expression along its directive axis[22,33,36], undermining the traditional association between radial body plans and diffuse neural organization.

Whether cnidarians can assemble discrete interneuron-like centers capable of local integrative processing has remained unclear. Here, using anatomical, molecular, and functional approaches, we examine nervous system organization in the cnidarian *Nematostella vectensis* and assess whether features associated with neural centralization extend deeper in animal evolution than previously appreciated.

Results

Motor coordination during feeding

Feeding, an innate, essential, and readily inducible behavior requiring whole-body coordination, provides a tractable entry point to test whether a cnidarian nerve net contains localized neural structures that support complex motor transitions. To characterize feeding under ecologically relevant conditions, we recorded adult *Nematostella* polyps partially burrowed in gravel with the oral disc exposed above the substrate (Fig. 1b). Upon introduction of free-swimming *Artemia* nauplii (brine shrimp larvae), tentacles that made contact bent, twisted, and captured prey, whereas non-contacting tentacles remained poised in the background. Prey-bearing tentacles then contracted toward the oral opening, conveying food through the pharynx and into the body cavity (Supplementary Video 1).

In initial experiments, we found that feeding responses were highly flexible and context dependent, varying with prey size, number, position, and mode of delivery (Supplementary Videos 2–5 and Supplementary Fig. 5f). To identify the core elements within this behavioral diversity, we established a simplified feeding paradigm in which a cylindrical egg-white pellet (1 mm × 1 mm) was gently delivered to the oral disc using a cat whisker (Fig. 1c,d and Supplementary Video 6). This consistently triggered a reproducible sequence of motor subroutines involving distinct body regions. We defined two stereotyped phases: (1) grasping, from the first tentacle-driven movement to the onset of neck constriction, during which tentacles sense and ensnare the pellet, pull it toward the mouth, and clasp around it; and (2) swallowing, from the onset of neck constriction until the pellet reaches the distal end of the pharynx, characterized by rhythmic neck contractions, mouth opening and closing, food passage through the pharynx, and temporary suspension of oral-to-aboral peristalsis. Our observations thus demonstrate that *Nematostella* executes a structured, multi-step feeding program despite lacking any obvious anatomical centralization.

Anatomical organization of the oral nerve net

The adaptability and robustness of feeding under varied conditions raise the question of how coordinated behaviors can be directed by a diffuse nerve net. In *Nematostella*, a previously described *NvElav1* reporter labels neurons along the body column[25] but

126 shows little expression in neurons of the oral disc and tentacles. To overcome this
127 limitation, we generated additional reporter lines by screening promoters of candidate
128 genes identified in scRNA-seq data[28].
129
130 Among them, a 1.9 kb upstream fragment of the *Nematostella SH3GL3* (Endophilin-A3)
131 homolog drove a fluorescent reporter *NvSH3GL3*^{P}*>mScarlet-I* (Fig. 2b) that robustly
132 labeled neurons, including dense innervation of the oral disc and tentacles, major
133 structures involved in feeding (Fig. 1e). Notably, this pattern resembles early hand-
134 drawn descriptions of oral neuronal condensations in other sea anemones[7,8], suggesting
135 that it may represent a conserved anatomical feature.
136
137 High-resolution imaging of the oral region revealed that neuronal organization is not
138 diffuse but rather exhibits pronounced spatial patterning in both soma distribution and
139 neurite orientation (Fig. 1e). Neurons with enlarged somata and multipolar morphology
140 clustered at tentacle junctions, where they gave rise to prominent circumferential neurite
141 bundles that together formed a ring-like structure. We refer to this neuronal structure as
142 the oral nerve ring (ONR). In contrast, other oral neurons exhibited smaller somata and
143 distinct projection orientations, including radially oriented neurites around the mouth and
144 longitudinal projections within the tentacles (Fig. 1e). With circumferential neurites
145 linking tentacles and localization at the interface between the tentacles, pharynx, and
146 body column, the ONR occupies a position well suited for coordinating activity across
147 multiple body regions.
148
149 To examine how this circumoral organization arises, we analyzed *NvSH3GL3*^{P}-labeled
150 neurons during larval-to-polyp transitions associated with tentacle formation (Fig. 2a,c).
151 In late planula larvae, neurons with enlarged somata were present but sparsely
152 distributed within the oral ectoderm and did not exhibit a coherent ring-like arrangement.
153 As animals progressed through the tentacle-bud stage and into primary polyps, the
154 number of these ONR neurons increased, accompanied by higher neurite density and
155 preferential localization to tentacle junctions (Fig. 2c). With further growth and the
156 sequential addition of tentacles[36], this process gave rise to a progressively denser

157 circumoral neurite bundle and an increased accumulation of large neuronal somata at
158 tentacle junctions, ultimately forming a clearly defined oral nerve ring (Fig. 2d). These
159 observations indicate that ONR organization emerges gradually during development
160 and scales with increasing body size and morphological complexity.
161
162 **Molecular diversity of the oral nerve net**
163 Building on the anatomical and developmental characterization of the oral nerve ring,
164 we next examined its molecular composition to assess potential functional
165 specialization. Oral discs from adult *NvSH3GL3*^{P} reporter animals were dissected, and
166 mScarlet-I-positive cells were enriched by fluorescence-activated cell sorting (FACS)
167 prior to single-cell RNA sequencing using the 10x Genomics platform (Fig. 3a). This
168 yielded 3,297 cells comprising both neural and non-neural populations (Fig. 3b), as
169 defined by marker gene expression (Fig. 3c). Specifically, neural clusters expressed
170 canonical neuronal markers (*ELAV*, *achaete-scute*), synaptic machinery (*synapsin*,
171 *synaptotagmin*, *endophilin*, vesicular transporters), as well as cytoskeletal proteins, ion
172 channels, transporters, and adhesion/signaling molecules (Fig. 3c and Supplementary
173 Fig. 1a). Expression of the *NvSH3GL3*^{P} reporter closely paralleled endogenous
174 *NvSH3GL3* across neural clusters, supporting the fidelity of the reporter. In contrast,
175 non-neural clusters expressed the endogenous red fluorescent protein *NvFP-7R*[37]
176 together with tissue-associated cytoskeletal and extracellular-matrix genes, providing an
177 internal reference for non-neural identity (Fig. 3c).
178
179 To examine the spatial expression of markers enriched in specific transcriptional
180 clusters, we analyzed four-tentacle primary polyps (7–10 days post-fertilization, dpf),
181 which are more amenable to whole-mount fluorescent in situ hybridization (FISH) and
182 confocal imaging than adult tissues. Markers enriched in cluster 3 consistently localized
183 to the pharyngeal region (Fig. 3d,e). In contrast, markers enriched in clusters 5 and 6
184 localized predominantly to the ectoderm of the oral disc and tentacles (Fig. 3f,g and
185 Supplementary Fig. 1b–e). Together, these findings show that at least a subset of
186 transcriptionally defined neural clusters within the oral nerve net exhibit clear spatial
187 correlates across oral tissues, linking molecular identity to anatomical position.

188

189 **Interneuron-like molecular features of the oral nerve ring**

190 We next examined the molecular diversity of oral neurons, as reflected in their sensory
191 transduction components and neurotransmitter receptor repertoires, to assess whether
192 transcriptionally defined populations exhibit features consistent with functional
193 specialization. Sensory-related genes included acid-sensing ion channels (ASICs),
194 transient receptor potential (TRP) channels, opsins, and cilia-associated proteins
195 (CFAPs, DNAHs, and RSPs). Neurotransmitter receptors fell into three classes:
196 excitatory (ionotropic glutamate, acetylcholine), inhibitory (ionotropic GABA, glycine),
197 and modulatory (metabotropic glutamate, acetylcholine, GABA, monoamines,
198 neuropeptides). Full gene lists are provided in Supplementary Table 2.

199

200 Comparison across transcriptional clusters revealed that clusters 5 and 6 were
201 distinguished by low sensory gene expression and broad representation of excitatory
202 (E), inhibitory (I), and modulatory (M) receptor classes (Fig. 4a). Co-expression analysis
203 showed that the majority of cells within these clusters simultaneously expressed
204 receptors from all three classes (Fig. 4b and Supplementary Fig. 2), indicating a
205 molecular profile consistent with integrative signal processing rather than sensory
206 specialization, reminiscent of integrative interneurons in the bilaterian CNS. This
207 molecular profile also mirrored two morphological features observed in ONR neurons
208 labeled by the *NvSH3GL3*^{P} reporter, including the absence of sensory cilia and the
209 presence of ganglion-like neuronal condensations. Although clusters 5 and 6 shared
210 these general characteristics, their receptor compositions diverged. Cluster 5 exhibited
211 substantial heterogeneity in E/I/M receptor combinations, whereas cluster 6 displayed a
212 more uniform and balanced receptor profile across cells (Fig. 4c). This balance,
213 approximately 20–30–50 in the relative proportions of excitatory, inhibitory, and
214 modulatory receptor expression per cell, was maintained despite variation in receptor
215 identity, suggesting functional convergence within cluster 6.

216

217 Other oral neural clusters differed from clusters 5 and 6 by showing sensory and/or
218 modulatory biases rather than integrative receptor profiles. Cluster 9 exhibited a

219 sensory bias, expressing receptors from all three classes, but with most cells single- or
220 double-positive and enriched for sensory and ciliary genes (Fig. 4a,b). Clusters 11, 12,
221 and 14 displayed a combined sensory and modulatory bias, characterized by distinct
222 modulatory receptor expression at the cluster level (Supplementary Fig. 3a) and, at the
223 single-cell level, by co-expression of broad sets of modulatory receptor genes together
224 with sensory-related genes (Fig. 4a and Supplementary Fig. 3b–d). Despite these
225 receptor-rich profiles, none of these clusters exhibited the balanced E/I/M co-expression
226 pattern that distinguishes clusters 5 and 6 (Fig. 4a–c).
227
228 Marker analysis further reinforced these distinctions (Fig. 4d). Clusters 5 and 6 shared
229 transcription factors including *POU4/Brn3*[29], *Orthopedia (Otp)*, and *SIX3/6*[27], which are
230 known to regulate anterior CNS patterning and neuronal specification in Bilateria[38–40].
231 Although *SIX3/6* expression is restricted to the aboral pole in *Nematostella* larvae[27], it
232 was enriched in adult oral disc neurons (Supplementary Fig. 1b). Both clusters also
233 expressed multiple ionotropic GABA receptor-like subunits, with shared and cluster-
234 specific paralogs (Fig. 4d and Fig. 6a), indicating subtype-specific inhibitory tuning. By
235 contrast, cluster 2 showed broad neuronal gene expression without defining markers,
236 consistent with an undifferentiated state. Together, these comparisons identified
237 clusters 5 and 6 as the most plausible ONR-associated neuronal populations within the
238 broader oral neural domain, based on their spatial localization and interneuron-like
239 molecular profiles.
240
241 To identify molecular markers within clusters 5 and 6 that label ONR neurons, we
242 performed FISH on four-tentacle primary polyps for genes enriched in these clusters.
243 Candidate genes were excluded from further consideration if they fell into three
244 categories that limited their utility as ONR markers: (1) genes enriched in the adult oral
245 disc scRNA-seq dataset but weak or undetectable in primary polyps (Supplementary
246 Fig. 1b); (2) transcripts detected in ONR-like cells but also expressed broadly along the
247 body column (Supplementary Fig. 1c,d); and (3) transcripts confined to the oral end but
248 either diffusely expressed across tissues or localized to cells lacking the large somata
249 and tentacle-junction positioning characteristic of ONR neurons (Supplementary Fig.

250 1e). By contrast, multiple ionotropic GABA receptor-like ($GABA_AR$-like) subunits
251 satisfied both transcriptional enrichment and anatomical localization criteria, with
252 expression concentrated in the oral region and in cells with ONR-like morphology (Fig.
253 3g, Fig. 6b, and Supplementary Fig. 1d). Although no single gene exclusively marked
254 the entire ONR, these results highlight GABA signaling as a promising entry point for
255 molecular and functional interrogation of the ONR.
256
257 **GABAergic pathway in the oral nerve net**
258 Building on this molecular signature, we asked whether the ONR contains the core
259 components of GABAergic signaling. In bilaterians, canonical GABAergic signaling
260 involves four key elements: synthesis by glutamate decarboxylase (GAD), vesicular
261 packaging by vesicular GABA transporter (VGAT), reception through ionotropic or
262 metabotropic GABA receptors, and clearance by GABA transporter (GAT)[41]. To assess
263 whether *Nematostella* possesses a comparable pathway architecture, we combined
264 immunohistochemistry, single-cell and bulk transcriptomics, and comparative genomics.
265
266 Whole-mount immunostaining of *NvSH3GL3*^{P}*>mScarlet-I* primary polyps revealed
267 widespread GABA immunoreactivity, with strong enrichment at the oral end (Fig. 5a).
268 Within the oral disc, a subset of GABA-positive cells overlapped with mScarlet-I-positive
269 neurons possessing large somata characteristic of ONR morphology (Fig. 5b),
270 suggesting that ONR neurons may both release and respond to GABA.
271
272 In our scRNA-seq dataset, among vesicular inhibitory amino acid transporter
273 (VIAAT) homologs, only a single homolog showed substantial expression in adult oral
274 neurons (LOC5506413; hereafter *VGAT*). Multiple $GABA_AR$-like subunits showed
275 expression largely confined to clusters 5 and 6 (Fig. 4d). Individual cells co-expressed
276 1–10 subunits (Fig. 4a), a combinatorial diversity rarely seen in invertebrates but
277 characteristic of the vertebrate CNS[41,42]. Subunits displayed broad to cluster-specific
278 distributions, with mutually exclusive, partially overlapping, or nested expression
279 patterns (Fig. 6a), consistent with cell type-specific receptor assemblies. Notably,
280 approximately 50% of cluster 5 neurons and 75% of cluster 6 neurons co-expressed

281 $GABA_AR$(s) and *VGAT* (Supplementary Fig. 5a), a defining feature of inhibitory
282 interneurons capable of both releasing and responding to GABA[41]. Some $GABA_AR$-
283 positive neurons lacked *VGAT*, likely representing postsynaptic targets of inhibition.
284 Together, these findings indicate that the ONR supports a GABAergic signaling
285 architecture encompassing both presynaptic and postsynaptic components, with
286 receptor diversity suggesting a capacity for fine-tuned inhibition comparable to bilaterian
287 central circuits.
288
289 To complement the single-cell RNA-seq data, we used bulk RNA-seq to transcriptionally
290 profile the adult tentacles, oral disc, pharynx, and oral body wall. This approach
291 provided deeper and less biased transcript coverage across whole tissues than scRNA-
292 seq restricted to FACS-enriched oral neurons. $GABA_AR$-like transcripts showed highest
293 relative expression in the oral disc and tentacles, mirroring GABA immunostaining and
294 reinforcing the receptor diversity of the oral nerve net (Fig. 5c).
295
296 Prompted by this enrichment, we surveyed the full *Nematostella* $GABA_AR$-like gene set.
297 Here, we use "$GABA_AR$-like" to denote subunits with sequence similarity to bilaterian
298 $GABA_A$ or glycine receptor subunits, as detailed in the Methods. Genomic analysis
299 identified 40 distinct subunits in *Nematostella*—exceeding the 2–23 typical of bilaterians
300 (Fig. 5d and Supplementary Table 4). Phylogenetic analysis across 13 species (7
301 cnidarians and 6 bilaterians; Supplementary Table 5) supported a single ancestral
302 $GABA_AR$, with subsequent expansions in both lineages (Fig. 5e and Supplementary Fig.
303 4). In *Nematostella,* only three subunits clustered with bilaterian orthologs, whereas the
304 remaining 37 arose from anthozoan-specific duplications, generating a lineage-specific
305 expansion that underpinned ONR receptor diversity. A recent preprint reported a similar
306 cnidarian-specific radiation based on narrower taxon sampling (2 cnidarians and 3
307 bilaterians) and functional assays of selected subunits[43]. Although metabotropic GABA
308 receptors are also expanded (12 in *Nematostella* vs. 2 in humans; Supplementary Table
309 4), their expression was scattered across neural and non-neural clusters without ONR
310 enrichment; therefore, we focused on ionotropic receptors as the core ONR-associated
311 repertoire.

312

313 Despite the presence of both plasma membrane (GAT) and vesicular (VGAT/VIAAT)
314 GABA transporters, and a diverse repertoire of GABA receptors, we did not identify a
315 canonical *GAD* homolog enriched in neuronal populations within the oral scRNA-seq
316 dataset. Ten putative *GAD*-like candidates, including two reported previously[44,45],
317 showed no enrichment in any neuronal cluster and were instead weakly or sparsely
318 expressed in a small number of non-neural clusters (Supplementary Table 6 and
319 Supplementary Notes). These findings suggest that GABA production in *Nematostella*
320 may rely on non-canonical or lineage-divergent pathways.

321

322 **A $GABA_A$ receptor-like subunit regulates swallowing initiation**

323 The molecular profiling described above highlights GABA signaling as central to ONR
324 function. Among the 40 $GABA_A$R-like homologs encoded in the *Nematostella* genome,
325 we focused on *NvGABAAR1* (LOC5505184), which showed the broadest expression
326 within cluster 5 and the highest transcript levels (Fig. 6a). *NvGABAAR1* was also co-
327 expressed with *VGAT*, a canonical feature of inhibitory interneurons. Moreover, it was
328 one of only three $GABA_A$R subunits that clustered with bilaterian orthologs (Fig. 5e), and
329 AlphaFold modeling revealed strong structural similarity to human GABRR3 (Fig. 5f and
330 Supplementary Fig. 5c). Crucially, FISH confirmed that *NvGABAAR1* was expressed in
331 oral disc neurons with large somata and circumferential neurites, consistent with ONR
332 morphology, although expression was also observed in a subset of tentacle neurons
333 (Fig. 6b).

334

335 To test the function of *NvGABAAR1*, we used CRISPR/Cas9 mutagenesis to introduce
336 a +27 bp insertion, generating a premature stop codon in the ligand-binding domain
337 (Supplementary Fig. 5b). Homozygous *NvGABAAR1*$^{+27/+27}$ animals were viable and
338 displayed no overt neural or developmental defects (Fig. 6c).

339

340 We next assayed the behavior of *NvGABAAR1*$^{+27/+27}$ mutants using our standardized
341 feeding paradigm. Animals were sequentially presented with four sham prey items (1
342 mm × 1 mm egg-white pellets), and grasping and swallowing durations were quantified

(Fig. 6d). Grasping duration, defined as the interval from the first tentacle-driven movement to the onset of neck constriction (Fig. 1d), did not differ between wild-type (WT) and mutant animals ($p = 0.35$), indicating intact prey detection and initial motor responses (Fig. 6e). Grasping duration was also stable across repeated trials for both genotypes, with no evidence of systematic drift over ten consecutive presentations (Supplementary Fig. 5d).

By contrast, swallowing showed a genotype-dependent effect restricted to the first of four feeding trials (Fig. 6f). Linear mixed-effects modeling revealed a significant genotype × trial interaction. Strikingly, WT animals showed stable swallowing durations across trials, whereas mutants exhibited a delay on the first feeding trial (46 ± 10 s; $p < 0.001$) and were indistinguishable from WT on subsequent trials (all $p > 0.2$). Importantly, including food-delivery method (pipette vs whisker) or starvation level as covariates did not alter the genotype × trial interaction, indicating that the delay on trial 1 reflects a robust, intrinsic deficit in swallowing initiation rather than an effect of stimulus delivery or feeding state. Mutant animals recovered rapidly after the initial trial and maintained WT-like swallowing durations for the remainder of the assay, a pattern that persisted for at least nine consecutive trials (Supplementary Fig. 5e). Together, these findings demonstrate that *NvGABAAR1* is specifically required for the initiation of swallowing behavior, supporting a role for GABAergic signaling within the oral nerve net in coordinating the transition from prey capture to ingestion and, potentially, the engagement of feeding-related behavioral states.

Discussion

Cnidarian nerve nets have long been viewed as diffuse and reflexive, yet their capacity for structured, context-dependent behaviors hints at deeper organization. Here we show that the sea anemone *Nematostella vectensis* possesses an oral nerve ring (ONR), a localized neural structure implicated in motor coordination during feeding. This finding suggests that key elements of neural integration predate the cnidarian–bilaterian split some 700 million years ago, extending the evolutionary roots of centralized organization.

374

375 The ONR forms a localized aggregation of neuronal somata that meets classical criteria
376 for a ganglion-like structure. In bilaterians, ganglia are clusters of somata functioning as
377 local integrative or relay centers, whereas in cnidarians “ganglion cells” traditionally
378 refer to aciliate neurons positioned basally within the epithelium[2,25]. Unlike previously
379 described neurite condensations in cnidarian nerve nets[25,46,47], the ONR constitutes a
380 true ganglion-like aggregation of neuronal somata, providing the first modern evidence
381 of soma-level clustering in a cnidarian (Fig. 1e). We use “ganglion-like” here in the
382 morphological sense only, to describe neuronal clustering rather than positional
383 homology to bilaterian ganglia. This clustered architecture provides an anatomical basis
384 for a CNS-like site of integration within a diffuse nerve net. ONR neurons display
385 morphological diversity, including bipolar and tripolar forms, suggesting heterogeneity in
386 connectivity and function. Developmentally, the ONR arises from initially scattered
387 neurons that progressively cluster as polyps grow (Fig. 2c,d). This scaling of
388 organization with body size and muscular compartmentalization may reflect an adaptive
389 route toward more efficient long-range coordination, a pattern that parallels proposed
390 evolutionary transitions from diffuse to centralized networks across early metazoans[4].
391 While postsynaptic partners remain unmapped, the ONR’s position and organization
392 indicate an interneuron-like hub mediating sensory–motor coordination.
393

394 Molecular and functional evidence support an interneuron-like identity for ONR neurons.
395 Single-cell analyses show that ONR neurons lack sensory markers but express a
396 combinatorial set of excitatory, inhibitory, and modulatory receptors together with
397 transcription factors typical of bilaterian interneurons (Fig. 4a–d). This transcriptional
398 profile defines a CNS-like integrative module, in which prominent inhibitory components,
399 including GABA-immunoreactive somata, a vesicular GABA transporter, and an
400 expanded suite of $GABA_A$ receptor-like subunits, form a molecular framework for
401 regulating excitation balance and temporal precision[41]. Although comprehensive
402 functional mapping of the ONR remains beyond the scope of this study, our functional
403 perturbation of an ONR-enriched $GABA_AR$ subunit selectively delayed the onset of
404 swallowing behavior without impairing prey detection or grasping (Fig. 6e,f). The delay

was most evident during the first feeding event but normalized by the second trial, indicating rapid behavioral recovery once feeding was initiated. This transient phenotype suggests that the ONR contributes to the timing and coordination of motor transitions during the initial stages of feeding rather than executing the motor output itself. Future work may uncover how internal physiological states shape ONR-mediated coordination. Together, these observations point to a role for inhibitory signaling within the ONR in modulating behavioral sequence progression, a hallmark of integrative rather than purely reflexive circuits.

Intriguingly, ONR neurons also expressed *SIX3/6* and *Orthopedia* (Fig. 4d), two broadly conserved transcription factors that in bilaterians regulate anterior CNS patterning and neuroendocrine specification[39,40]. These findings suggest that transcriptional programs defining the bilaterian anterior neuroectoderm may have deep evolutionary roots in the patterning of neural condensations around feeding structures.

Collectively, our results position the *Nematostella* oral nerve ring as an intermediate level of neural organization between diffuse nerve nets and centralized nervous systems. Its architecture exemplifies how clusters of interneuron-like cells can enable coordination without a bona fide brain. The marked expansion of neurotransmitter receptors (Supplementary Table 2) underscores molecular elaboration as a route to circuit flexibility in early animals, perhaps through receptor repurposing or adaptive tuning to estuarine variability. While it remains unresolved whether the *Nematostella* ONR and bilaterian CNS share a common origin or represent convergent solutions, their shared features reveal deep evolutionary continuity in the principles of neural integration.

Methods

Animals and husbandry

Nematostella vectensis anemones were maintained in 12 parts per thousand (ppt) artificial seawater (ASW, Instant Ocean) in glass containers at room temperature (RT, ~22 °C) under low ambient light. Animals were fed freshly hatched *Artemia* nauplii 2–3 times per week, and seawater was replaced the following day to remove residual food and waste. Juvenile polyps were raised at 27 °C after their first feeding until sexual maturity, after which adults were kept long-term at either RT or 16 °C as needed. Mixed-sex populations were housed at the Stowers Institute and were originally derived from founder stock provided by Mark Martindale. Unless otherwise specified, all animals used in this study were kept under these standard conditions.

Spawning and embryo preparation

Spawning was induced following established *Nematostella* protocols[48,49]. Sexually mature adults were kept at 16 °C, then transferred to RT and placed in front of a light box overnight to induce gamete release. The following morning, dishes were cold-shocked by replacing the water with 16–18 °C 12 ppt ASW. Unfertilized egg sacs were collected for microinjection. Egg sacs were dejellied in 4% L-cysteine prepared in 12 ppt ASW and incubated for 10 min on a gentle rocker. Wide-bore transfer pipettes were used to minimize mechanical damage. Dejellied eggs were washed several times in ASW, transferred to clean dishes, and kept at 16 °C until microinjection or fertilization.

Fertilized embryos used for fluorescent in situ hybridization and developmental imaging were cultured at 24 °C in the dark under standard conditions. Developmental stages used in this study included planula larvae (3 days post-fertilization, dpf) and primary polyps (7–10 dpf). Primary polyps corresponded to the first sessile feeding stage and were unfed, four-tentacle animals within this early post-metamorphic window. Juveniles were staged by tentacle number. Adults were considered as sexually mature polyps, typically bearing 16 tentacles and older than three months.

462 **Transgenic line generation**

463 The *NvSH3GL3*^{P}*>mScarlet-I* reporter construct was designed using a 1.9 kb promoter
464 fragment upstream of the *NvSH3GL3* locus to drive an *mScarlet-I–CAAX–P2A–HaloTag*
465 reporter cassette followed by an SV40 polyadenylation signal. mScarlet-I fluorescence
466 was used for all anatomical imaging. The vector was assembled using the NEBuilder
467 HiFi DNA Assembly Master Mix (NEB, E2621) and sequence-verified prior to injection.
468 Oligonucleotides used for promoter cloning are listed in Supplementary Table 9.
469
470 Unfertilized oocytes were microinjected following established Meganuclease (I-SceI)-
471 mediated transgenesis procedures[21,50]. Injection mix consisted of 10× I-SceI buffer (10
472 mM Tris-HCl, 10 mM $MgCl_2$, 1 mM DTT, pH 8.8), ~50 ng μl^{-1} plasmid DNA, 0.4 U μl^{-1} I-
473 SceI enzyme (NEB, R0694), and FITC (Fisher Scientific, 46425) to visualize injection
474 boluses. The mixture was assembled and pre-incubated according to standard
475 protocol[21]. Microinjection was performed using an Eppendorf FemtoJet, and injected
476 oocytes were fertilized after the injection session (≤ 1 h). Embryos were kept at 18 °C
477 overnight and subsequently raised at RT with regular ASW changes until first feeding.
478
479 Injected animals retaining mosaic reporter expression after two feedings were pooled
480 and raised to adulthood. Individual F0 adults were crossed to wild-type (WT) animals to
481 assess germline transmission. A single F0 female carrier was identified and used to
482 establish the line. Reporter-positive F1 offspring were outcrossed to WT animals,
483 yielding ~50% reporter-positive F2 progeny maintained as a stable heterozygous
484 population. F2 reporter animals were used for all anatomical imaging and single-cell
485 applications. F3 animals were generated by intercrossing F2 individuals, and
486 homozygotes were identified by test-crossing to WT animals, which yielded 100%
487 reporter-positive progeny. Homozygous F3 animals were maintained as genetic stock.
488
489 For anatomical reference in selected live-imaging experiments, a previously generated
490 transgenic reporter expressing GFP under the control of the myosin heavy chain
491 promoter[51] was used to visualize muscle tissue. This reporter was used only for
492 qualitative anatomical comparison and was not employed for quantitative analyses.

493

494 **CRISPR/Cas9 mutant generation**

495 CRISPR/Cas9 genome editing was performed as previously described[20,52]. A single
496 guide RNA (sgRNA) targeting the *NvGABAAR1* coding sequence was designed using
497 the CRISPRscan server[53] (https://www.crisprscan.org/sequence/) with default
498 parameters (Cas9 - NGG, In vitro T7 promoter). The selected sgRNA targeted a site
499 within the ligand-binding domain. A double-stranded DNA template for sgRNA synthesis
500 was generated by annealing the gene-specific forward primer to a universal reverse
501 primer, followed by Klenow extension (37 °C for 30 min, 75 °C for 15 min; Klenow
502 Fragment, NEB, M0210). In vitro transcription was performed using the AmpliScribe T7-
503 Flash Transcription Kit (Biosearch Technologies, ASF250) at 37 °C for 5 h, followed by
504 DNase I treatment for 15 min. The sgRNA was purified using the Direct-zol RNA
505 MiniPrep Kit (Zymo Research, R2052) according to the manufacturer's instructions and
506 quantified using a NanoDrop spectrophotometer (Thermo Fisher Scientific).

507

508 For microinjections, Cas9 protein with NLS (PNA Bio, CP02) was mixed with sgRNA at
509 equal concentrations and diluted to 500 ng μl^{-1} each in nuclease-free water. FITC
510 (Fisher Scientific, 46425) was added to visualize injection boluses. Unfertilized oocytes
511 were injected with Cas9–sgRNA complexes, fertilized with WT sperm following the
512 injection session, and raised at RT.

513

514 To evaluate editing efficiency and identify potential founders, a subset of injected
515 embryos was sacrificed at 3–10 dpf for genotyping, since their small size precludes non-
516 lethal tissue sampling. The remaining injected siblings were raised to adulthood as
517 candidate F0 animals. A single F0 male was identified as carrying a +27 bp insertion,
518 resulting in a premature stop codon within the ligand-binding domain of *NvGABAAR1*.
519 This F0 male was crossed to a homozygous F3 *NvSH3GL3*^{P}*>mScarlet-I* reporter
520 female, and genotyping of 3–10 dpf F1 offspring confirmed germline transmission of the
521 +27 allele. The remaining F1 siblings were raised to juvenile stages and individually
522 genotyped to identify heterozygous *NvGABAAR1*$^{+/+27}$, reporter-positive individuals. All
523 such F1 animals were pooled and intercrossed to generate the F2 generation.

524

525 Individual F2 animals were genotyped to distinguish reporter-positive WT
526 (*NvGABAAR1*$^{+/+}$), heterozygous (*NvGABAAR1*$^{+/+27}$), and homozygous
527 (*NvGABAAR1*$^{+27/+27}$) siblings. F3 WT controls were generated by intercrossing reporter-
528 positive F2 WT siblings (*NvGABAAR1*$^{+/+}$ × *NvGABAAR1*$^{+/+}$), and F3 homozygous
529 mutants were generated by intercrossing reporter-positive F2 homozygous siblings
530 (*NvGABAAR1*$^{+27/+27}$ × *NvGABAAR1*$^{+27/+27}$). All neural-morphology imaging and
531 behavioral assays were conducted on F3 homozygous mutants together with their F3
532 WT siblings. Throughout, “wild-type” refers to same-generation siblings lacking the +27
533 allele rather than unrelated WT animals.
534

535 For genotyping, whole embryos (<10 dpf) or aboral tissue from juveniles and adults was
536 lysed in QuickExtract DNA Extraction Solution (Biosearch Technologies, QE09050) at
537 65 °C for 30 min and 98 °C for 2 min. The *NvGABAAR1* target locus was amplified by
538 PCR, followed by a second round of amplification to introduce sample-specific dual
539 barcodes. Amplicons were pooled and size-selected using the ProNex Size-Selective
540 Purification System (Promega), quantified on a Qubit Fluorometer (Thermo Fisher
541 Scientific), and assessed for size and purity on an Agilent Bioanalyzer. Purified pools
542 were sequenced on an Illumina MiSeq 2 × 250 bp flow cell. The resulting sequence data
543 were demultiplexed, read pairs were joined, and indel frequencies and allele identities
544 were analyzed using CRIS.py[54].
545

546 All primers used for sgRNA template generation and genotyping are listed in
547 Supplementary Table 9.
548

549 **Behavioral assays**

550 *Animal preparation*

551 Adult F3 *NvGABAAR1*$^{+27/+27}$ mutants and their WT siblings were used for all behavioral
552 experiments. Animals were ~1 year post-fertilization and of comparable size; unusually
553 large or small individuals were excluded. Because *Nematostella* lacks reliable external

554 sex markers and no sex-specific differences in feeding behavior are known, mixed-sex
555 animals were used.
556
557 Mutant and WT groups were maintained separately at RT in Pyrex glass dishes under
558 low ambient light, as described above, and kept on the same shelf to minimize
559 environmental variation. Animals were fed freshly hatched *Artemia* once per week. To
560 avoid physiological effects of high-protein or non-native food sources (such as egg
561 white), feeding assays were spaced by at least 4 weeks of routine *Artemia* feeding.
562
563 For each experiment, individual animals were transferred 2–4 days before the assay
564 into sterile 60 × 15 mm polystyrene dishes (Falcon 351007) containing 12 ppt ASW and
565 allowed to acclimate to the brighter ambient illumination near the imaging setup.
566 Seawater was replaced the night before or morning of the assay to remove gametes
567 and metabolic waste. On the day of testing, dishes were placed next to the imaging
568 setup for ≥ 1 h so animals could fully relax and extend under the recording illumination,
569 which was essential to prevent retraction during dish handling and the assay.
570
571 Animals were assayed 7, 11, or 14 days after their last *Artemia* feeding, with 14-day
572 animals representing the more strongly starved condition. Mutant and WT animals from
573 the same cohort were always tested in parallel on the same day, and datasets pooled
574 measurements from multiple independent assay days.
575
576 *Food preparation*
577 For qualitative behavioral observations, *Artemia* nauplii were used for naturalistic
578 feeding (Supplementary Video 1), whereas mussel tissue, torn into small pieces with
579 fine forceps, was used for assays involving multiple food items, lateral presentation, and
580 sequential feeding (Supplementary Videos 3–5).
581
582 For assays involving standardized food geometry, cylindrical egg-white pellets were
583 prepared from the white portion of hard-boiled chicken eggs (Supplementary Videos 2
584 and 6). Egg-white slices (5–8 mm thick) were cored using an EMS Core Sampling Tool

585 (EMS 69039) and gently pressed into a soft substrate to avoid compression artifacts,
586 generating cylindrical logs. Logs were then cut into pellets with height equal to diameter
587 using a 0.125-mm ultra-fine tungsten dissecting needle (Roboz Surgical RS-6063).
588 Pellets of 0.5, 0.75, 1.0, 1.2, 1.5, and 2.0 mm diameter were used for size-series
589 comparisons (Supplementary Video 2). A diameter of 1.0 mm was selected for all
590 quantitative assays (Supplementary Video 6), as smaller pellets were difficult to track
591 and did not reliably elicit mouth opening, whereas larger pellets introduced variability
592 due to prolonged and inconsistent transit through the pharynx.
593
594 *Food delivery*
595 Food pellets were delivered by either a pipette- or whisker-based approach. In the
596 pipette method, a pellet was released from a glass Pasteur pipette positioned adjacent
597 to a tentacle near the oral opening. Glass pipettes were required because plastic
598 pipettes caused egg-white pellets to adhere to the inner surface and impeded reliable
599 release. This method produced a slight water disturbance, providing both mechanical
600 and chemical cues. In the whisker method, the pellet was first released distally in the
601 dish and then gently guided toward the oral opening using a trimmed cat whisker affixed
602 to a wooden toothpick. The whisker provided sufficient rigidity for precise manipulation
603 while introducing minimal mechanical stimulation. This method enabled more consistent
604 placement of the food stimulus, although grasping onset was typically slower and more
605 variable due to reduced mechanical cues relative to pipette delivery.
606
607 For swallowing analyses, pipette- and whisker-delivered trials were pooled because the
608 delivery method did not significantly affect swallowing durations within each genotype.
609 This was confirmed by the linear mixed-effects models (see Supplementary Table 8).
610 Parallel to these findings, while delivery method influenced grasping durations, the
611 effect was comparable across genotypes (Supplementary Fig. 5f).
612
613 *Feeding assay*
614 Dishes containing single acclimated animals were arranged beside the imaging setup
615 and moved into view with minimal disturbance. All assays were recorded. Food pellets

were delivered by either the pipette or whisker method, as described above. After a pellet was grasped and swallowed, the next trial began only once the ingested pellet had fully passed through the pharynx into the gastrovascular cavity and no further downward movement was observed.

A trial was defined as one pellet presentation and the resulting grasping and swallowing sequence. Each behavioral session (one animal per session) consisted of 4–10 sequential trials, but only the first four consecutive trials (trials 1–4) were used for quantitative analyses. Grasping and swallowing latencies showed no systematic change after the first three trials, and additional trials increased the likelihood of movement artifacts or handling disturbances.

Sessions were excluded if swallowing was accompanied by pronounced bending of the oral region, which mechanically altered ingestion dynamics. Such bending was typically triggered when a centrally delivered pellet was captured by a peripheral tentacle. To avoid these artifacts, any peripheral capture within trials 1–4 led to exclusion of the session. Peripheral capture occurring only after trial 4 did not affect inclusion, as later trials were not analyzed. Sessions were also terminated if the animal retracted into its body column during the assay, even if it later re-extended. Animals with unusually narrow pharynges were excluded to prevent anatomical constraints from influencing timing measurements.

Video acquisition

Behavioral sessions were recorded on a Leica M165 FC stereo microscope equipped with a Flexacam C1 camera. Videos were acquired at 1× magnification and 0.73× zoom, at either 0.50 or 0.87 s/frame.

Behavior annotation

Grasping and swallowing were quantified from time-lapse recordings as two sequential phases of the feeding response. For quantification, grasping was defined as the period from the first tentacle-driven engagement of the pellet to the onset of neck constriction,

and swallowing as the period from the initiation of neck constriction to the moment the pellet reached the distal end of the pharynx.

For each trial, three frames were manually identified in Fiji:
t1 — first clear grasping movement after pellet introduction, marked by the onset of a tentacle-driven pull toward the mouth.
t2 — beginning of neck constriction, often coinciding with or following a tentacle clasping motion.
t3 — frame in which the pellet reached the distal end of the pharynx. This endpoint was used because the time from this point to entry into the gastrovascular cavity varied widely across trials and individuals.

Grasping and swallowing durations were calculated as the frame difference multiplied by the corresponding seconds-per-frame value: $T_{grasp} = (t2 - t1) \times s/frame$ and $T_{swallow} = (t3 - t2) \times s/frame$. Frame numbers and timestamps were recorded in Excel for downstream analysis. All trial-level grasping and swallowing duration measurements are provided in Supplementary Table 7.

Visualization and statistics

Data processing and visualization were performed in R (v4.4.1) using ggplot2 (v3.5.2) and standard tidyverse packages. Individual trial trajectories were plotted as faint lines, and genotype-wise mean ± s.e.m. were overlaid as solid lines. Grasping plots included pipette-delivery trials only, whereas swallowing plots included both pipette- and whisker-delivery methods.

All statistical analyses were performed in R. All statistical tests were two-sided. Feeding durations were analyzed using linear mixed-effects models fitted with lme4[55] (v1.1-38). AnimalID was included as a random intercept to account for repeated measurements from the same individual across trials. Fixed effects included genotype and trial number. For swallowing analyses, food delivery method and starvation duration were included as additional covariates.

678

679 Significance of main effects and interactions was assessed using Type III Analysis of
680 Variance (ANOVA) with Satterthwaite's method implemented in lmerTest[56] (v3.1-3).
681 Genotype differences at each trial were estimated using estimated marginal means and
682 pairwise contrasts computed with emmeans[57] (v2.0.0), utilizing the Kenward-Roger
683 approximation for degrees of freedom. The resulting estimates, standard errors,
684 confidence intervals, and p-values are provided in Supplementary Table 8. Statistical
685 inference relied on the assumptions of linear mixed-effects models; no additional tests
686 of normality or global multiple-comparison corrections were performed.
687

688 **Whole-mount staining**

689 Whole-mount staining was performed following previously published protocols[58] for
690 *Nematostella* with minor modifications. Planula larvae (3 dpf) and primary polyps (7–10
691 dpf) were collected into 1 ml ASW in round-bottom tubes. Primary polyps were allowed
692 to relax for ≥ 15 min, after which $MgCl_2$ was added stepwise by two sequential additions
693 of 100 µl of 7% $MgCl_2$ in 12 ppt ASW, with a 5-min incubation between additions.
694 Planula larvae were immobilized by adding 7% $MgCl_2$ directly, without a relaxation
695 period. After immobilization, the solution was removed and replaced with fixative.
696

697 For visualization of F-actin in fixed transgenic reporter animals, samples were fixed in
698 4% paraformaldehyde (PFA) in 12 ppt ASW for 1 h at RT with gentle rocking, followed
699 by washing 5 × 5 min in phosphate-buffered saline (PBS) containing 0.1% Tween-20
700 (PBTw). Samples were then incubated overnight at 4 °C on a shaker with either Alexa
701 Fluor 488-conjugated phalloidin (1:300) or SiR-actin (Cytoskeleton, CY-SC001; 1:1000),
702 washed again in PBTw, and cleared by immersion in ScaleA2 (2 M urea, 75% glycerol
703 in water) prior to mounting and imaging.
704

705 For GABA immunostaining, animals were fixed for 3 min in 4% PFA supplemented with
706 0.05% glutaraldehyde in 12 ppt ASW, followed by post-fixation in 4% PFA in 12 ppt
707 ASW for 1 h at room temperature with gentle rocking. Samples were washed 5 × 5 min
708 in PBTw and incubated in blocking buffer (PBTw supplemented with 5% normal goat

709 serum, 1% bovine serum albumin, and 10% dimethyl sulfoxide [DMSO]) for 2 h at RT.
710 Primary antibody incubation was performed overnight at 4 °C on a shaker using rabbit
711 anti-GABA (Sigma-Aldrich, A2052; 1:500) diluted in blocking buffer without DMSO. The
712 following day, samples were washed 6 × 20 min in PBTw and incubated overnight at
713 4 °C on a shaker with goat anti-rabbit Alexa Fluor 647 secondary antibody (Invitrogen,
714 A-21245; 1:1000) diluted in blocking buffer without DMSO. Samples were then washed
715 6 × 20 min in PBTw and cleared in ScaleA2 prior to imaging.
716
717 **Whole-mount fluorescent in situ hybridization**
718 Gene-specific probe regions were selected and verified for specificity by BLAST
719 searches against the *Nematostella* transcriptome. Nested PCR on cDNA templates
720 amplified the target region, and the second-round reverse primer incorporated a T7
721 promoter sequence for in vitro transcription. Final PCR products were Sanger-
722 sequenced to confirm identity. DIG-labeled antisense RNA probes were generated by in
723 vitro transcription using the DIG RNA Labeling Mix (Roche, 11277073910), followed by
724 DNase I treatment and column purification (Zymo Research, R2052). Primer sequences
725 used for probe generation are listed in Supplementary Table 9.
726
727 FISH was performed based on established *Nematostella* protocols[59]. In brief, animals
728 were immobilized as described for immunostaining, pre-fixed for 90 s in ice-cold 4%
729 PFA + 2.5% glutaraldehyde in 12 ppt ASW, and then fixed in 4% PFA in 12 ppt ASW for
730 1 h at RT. Samples were washed in PBS and dehydrated through a PBS/methanol
731 series into 100% methanol. Endogenous peroxidase activity was quenched in 3% H_2O_2
732 in 90% methanol for 1 h at RT, followed by rehydration through a methanol/PBS series.
733 Tissues were permeabilized with Proteinase K (20 µg ml^{-1} for 10 min), post-fixed in 4%
734 PFA for 1 h, washed in PBTw, and transitioned into hybridization buffer at 60 °C, where
735 they were pre-hybridized overnight. DIG-labeled probes (1 ng $µl^{-1}$) were denatured at
736 80 °C for 10 min, snap-cooled on ice, and hybridized to samples at 60 °C for 48 h. After
737 hybridization, samples were washed at 60 °C through SSC solutions of increasing
738 stringency, then returned to RT and washed into TNT (0.1 M Tris-HCl pH 7.5, 0.15 M
739 NaCl, 0.1% Tween-20). Samples were blocked in TNT containing 5% sheep serum and

740 1% blocking reagent (Roche) for 2 h at RT, then incubated overnight at 4 °C with anti-
741 DIG-POD Fab fragments (Roche, 11207733910; 1:1000). Fluorescent signal was
742 developed using the TSA Cyanine 3 system (Akoya, NEL704A001KT) for 20 min at RT.
743 After washing into PBTw, samples were counterstained with SiR-DNA (Cytoskeleton,
744 CY-SC007; 1:1000), cleared in ScaleA2, and mounted for imaging as described for
745 immunostaining.
746
747 **Imaging and image processing**
748 All samples were imaged on either a Nikon spinning-disk confocal system (20× or 40×
749 objectives) or an Andor Dragonfly spinning-disk confocal microscope (25× or 40×
750 objectives). Z-stacks were acquired at 1-µm step size. Maximum intensity projections,
751 orthogonal views generated by reslicing, and all subsequent image processing (rotation,
752 cropping, and linear min/max intensity scaling) were performed in Fiji for visualization.
753
754 **Single-cell RNA-seq**
755 *Tissue dissociation and cell sorting*
756 Adult F2 *NvSH3GL3*^{P}*>mScarlet-I* animals were used for the single-cell RNA-seq
757 experiment. All animals were of mixed sex, and the workflow was performed as a single
758 batch on the same day. Animals were fasted for five days and transferred from 16 °C to
759 RT for ~8 h before dissociation. Animals were kept in 12 ppt ASW until fully relaxed and
760 immobilized by gradually adding a 7% $MgCl_2$ solution prepared in ASW (Sigma-Aldrich,
761 M2670). Oral discs were dissected by a single transverse cut just below the pharynx,
762 with most tentacles trimmed away. Dissected tissues were briefly rinsed in Ca^{2+}/Mg^{2+}-
763 free ASW (154 mM NaCl, 3.57 mM KCl, 0.70 mM $NaHCO_3$, 2.33 mM Na_2SO_4; all salts
764 from Sigma-Aldrich), then briefly ground (~15 s) and gently triturated for ~20 min at RT
765 in Ca^{2+}/Mg^{2+}-free ASW containing L-cysteine (2 mg ml^{-1}; Sigma-Aldrich, 168149),
766 papain (4 mg ml^{-1}; Sigma-Aldrich, P4762), and Liberase TM (0.05 mg ml^{-1}; Roche,
767 5401119001). Cell suspensions were filtered through 30 µm filters (FILCONS 030-33s;
768 CTSV), pelleted (300 × g, 10 min, 4 °C), washed in enzyme-free Ca^{2+}/Mg^{2+}-free ASW,
769 and stained on ice for 5 min with DAPI (2 µg ml^{-1}; Sigma-Aldrich, D9542) and DRAQ5
770 (25 µM; Thermo Fisher Scientific, 62251).

771

772 Cells were analyzed and sorted on a BD Influx flow cytometer (100 µm nozzle, 20 psi).
773 Excitation and emission were collected for DAPI (345/455 nm), DRAQ5 (647/697 nm),
774 and mScarlet-I (578/613 nm). Because *Nematostella* oral tissue exhibits strong
775 autofluorescence from the endogenous red fluorescent protein NvFP-7R[37] (569/593
776 nm), gating was anchored using a fluorescence-minus-one (FMO) control prepared from
777 WT oral-disc cells stained with DAPI and DRAQ5 but lacking mScarlet-I. This control
778 captured the autofluorescence range of NvFP-7R and defined the background threshold
779 for the reporter channel. A tentacle sample expressing mScarlet-I but lacking NvFP-7R
780 established the mScarlet-I emission profile. Reporter-positive gates retained events
781 bright in the mScarlet-I detector and dim in an adjacent 670/30 channel, minimizing
782 NvFP-7R carryover. Only singlets and live, nucleated events ($DAPI^-/DRAQ5^+$) were
783 included. The final gate contained ~2% of total events in the reporter population versus
784 0.1% in the FMO control, yielding approximately 45,700 sorted events collected into
785 RNase-free tubes for single-cell RNA-seq.
786

787 *Library preparation and sequencing*

788 Dissociated and sorted cells were assessed for concentration and viability using a
789 LUNA-FL Cell Counter (Logos Biosystems). Samples with ≥ 90% viable cells were
790 loaded onto a Chromium Controller (10x Genomics), targeting recovery of ~3,200 cells.
791 Single-cell cDNA libraries were prepared with the Chromium Single Cell 3′ Reagent Kit
792 v3 (10x Genomics) according to the manufacturer's instructions. cDNA and final short-
793 fragment libraries were evaluated for quality and quantity using a 2100 Bioanalyzer
794 (Agilent Technologies) and a Qubit Fluorometer (Thermo Fisher Scientific). Libraries
795 were sequenced on an Illumina NextSeq 500 to a mean depth of ≥ 100,000 reads per
796 cell (paired-end 28 × 8 × 91 bp) using Real-Time Analysis (RTA) and instrument
797 software versions current at the time of sequencing.
798

799 FASTQ files were processed with Cell Ranger (v8.0.1; 10x Genomics,
800 https://www.10xgenomics.com/) against the *Nematostella vectensis* genome assembly
801 jaNemVect1.1 (GCF_932526225.1; NCBI RefSeq[60] Annotation Release 101),

802 supplemented with the *NvSH3GL3*^{P}*>mScarlet-I* reporter sequence. The resulting gene–
803 cell count matrix was analyzed in Seurat[61] (v5.1.0) in R (v4.4.1). Cells were retained if
804 they expressed 200–3,000 genes, contained ≤ 15,000 unique molecular identifiers
805 (UMIs), and exhibited < 5% mitochondrial gene content (identified from RefSeq-
806 annotated mitochondrial gene prefixes). Data were normalized with SCTransform[62], and
807 the top 3,000 most variable genes were used for principal-component analysis (PCA).
808 The first 15 principal components were used to construct a shared nearest-neighbor
809 graph (FindNeighbors) and perform graph-based clustering (FindClusters, resolution =
810 0.5). Uniform Manifold Approximation and Projection (UMAP) embeddings computed
811 from the same components were used for visualization.
812
813 *Clustering and analysis*
814 Cluster identities were assigned by examining marker genes identified with
815 FindAllMarkers and cross-referenced with manually curated *Nematostella* gene sets for
816 neuronal developmental, synaptic function, sensory transduction, and neurotransmitter
817 receptors (Supplementary Tables 1 and 2). These curated lists were generated from
818 NCBI RefSeq annotations using keyword-based filtering and provided the framework for
819 assigning biologically meaningful identities to each cluster.
820
821 Gene-set quantification was performed using the same manually curated gene lists.
822 Expression was evaluated from the SCT-normalized count layer, and a gene was
823 considered detected in a cluster if it exhibited non-zero expression and was expressed
824 in more than 10% of cells in that cluster. For each gene set, per-cluster counts of
825 detected genes and per-gene summary tables (average expression, percent of
826 expressing cells, and annotation metadata) are provided in Supplementary Table 2.
827
828 All visualizations were generated in R using Seurat (v5.1.0), ggplot2 (v3.5.2), ggtern
829 (v3.5.0), pheatmap (v1.0.12), patchwork (v1.3.0), and standard tidyverse packages. All
830 analysis and visualization code is available at [link].
831
832 **Bulk RNA-seq**

833 Adult male *Nematostella vectensis* polyps (n = 3 individuals) were dissected into four
834 tissue types (pharynx, body wall, proximal tentacles, and oral disc), yielding twelve total
835 samples (three biological replicates per tissue). Each tissue piece was immersed in 300
836 µl TRIzol reagent (Invitrogen, 15596026) and snap-frozen in liquid nitrogen before
837 storage at –80 °C. RNA was extracted using the Direct-zol RNA MiniPrep Kit (Zymo
838 Research, R2052) following the manufacturer's protocol, including a 15 min on-column
839 DNase I digestion to remove genomic DNA.
840
841 mRNA-seq libraries were generated from 100 ng (or < 100 ng for two samples) of high-
842 quality total RNA, as assessed using the Bioanalyzer (Agilent). Libraries were prepared
843 using the TruSeq Stranded mRNA Library Prep Kit (Illumina, 20020594) and TruSeq
844 RNA Single Indexes Sets A and B (Illumina, 20020492 and 20020493). Libraries were
845 purified using the AMPure XP bead-based reagent (Beckman Coulter, A63882),
846 evaluated for quality and quantity using the Bioanalyzer (Agilent) and Qubit Fluorometer
847 (Life Technologies). Equal-molar libraries were pooled, quantified, and sequenced as 75
848 bp paired-end reads on a mid-output flow cell using the NextSeq 500 (Illumina).
849 Following sequencing, demultiplexing and FASTQ generation were performed using
850 Illumina RTA (v2.4.11) and bcl2fastq2 (v2.20).
851
852 FASTQ files were aligned to the *Nematostella vectensis* genome assembly
853 jaNemVect1.1 (GCF_932526225.1; NCBI RefSeq[60] Annotation Release 101) using
854 STAR[63] (v2.7.10b) with quantMode GeneCounts to obtain gene-level counts. Alignment
855 summary rows were removed and raw counts were imported into R and analyzed with
856 edgeR[64] (v4.2.2). Lowly expressed genes were filtered using filterByExpr with tissue as
857 the grouping factor, and library sizes were normalized using the trimmed mean of M-
858 values (TMM) method. Gene lengths were obtained from the corresponding RefSeq
859 gene models and used to compute TPM values from the filtered count matrix
860 (Supplementary Table 3). For visualization, TPM values were averaged across
861 biological replicates for each tissue, restricted to a curated list of GABA receptor-like
862 subunits (Supplementary Table 4), and scaled per gene (row-wise) before generating
863 clustered heatmaps.

Phylogenetic analysis

Sequence identification and curation

Putative *Nematostella vectensis* γ-aminobutyric acid type A receptor ($GABA_AR$) and glycine receptor (GlyR) subunits were first identified by BLASTp[65] searches (v2.13.0+) against the *Homo sapiens* $GABA_AR$ and GlyR sequences and verified for domain composition using the InterPro server[66]. Although orthology between $GABA_AR$ and GlyR types remains unresolved in early-branching metazoans, no hits overlapped with nicotinic acetylcholine, 5-HT_3, or other members of the Cys-loop ligand-gated ion channel (LGIC) superfamily. These sequences are therefore collectively referred to as $GABA_AR$-like subunits throughout.

For *Nematostella*, candidate $GABA_AR$-like sequences were compiled from three curated sources: the NCBI RefSeq proteome[60,19] (https://www.ncbi.nlm.nih.gov/datasets/genome/GCF_932526225.1/) and two SIMRBase transcriptome-derived proteome assemblies[18] (NV2: wein_nvec200_tcsv2; NVE: wien_nvec200_v1; https://simrbase.stowers.org/starletseaanemone). Not all loci were represented across all datasets. When the same locus appeared in multiple sources, we retained the longest predicted amino-acid product; when sequences were equal in length, the RefSeq entry was selected. This procedure yielded 40 curated *Nematostella* $GABA_AR$-like subunits: 37 for which the RefSeq version was retained, 2 for which RefSeq lacked annotated protein entries and the longest ORFs were contributed by the NV2 assembly, and 1 for which the longest ORF was contributed by the NVE assembly, despite orthologous predictions also present in RefSeq and NV2 (Supplementary Table 4).

Homologous $GABA_AR$-like sequences for comparative phylogenetic analysis were retrieved from UniProt[67] (Swiss-Prot and TrEMBL; downloaded February 2024) for six bilaterian species (*Homo sapiens*, *Danio rerio*, *Drosophila melanogaster*, *Caenorhabditis elegans*, *Ciona intestinalis*, and *Octopus vulgaris*). The *Nematostella* and bilaterian sequences were used as queries for BLASTp[65] searches against six

895 additional cnidarian proteomes representing both anthozoans (*Acropora millepora*,
896 *Exaiptasia diaphana*, *Stylophora pistillata*) and medusozoans (*Clytia hemisphaerica,*
897 *Hydra vulgaris*, *Hydractinia symbiolongicarpus*). Resulting sequences from these
898 searches were further curated using CD-HIT[68,69] (v4.8.1) to remove redundant
899 sequences sharing ≥ 90 % similarity within each species. Protein database sources,
900 accession numbers, and annotations for all taxa are listed in Supplementary Table 5.
901
902 *Sequence alignment and phylogeny reconstruction*
903 The non-redundant candidates from all species were aligned with MAFFT[70] (v7.520)
904 using the L-INS-i algorithm, and discordant sequences were excluded after manual
905 inspection. Domain composition was re-evaluated using the InterPro server[66]
906 (https://www.ebi.ac.uk/interpro/search/sequence/, accessed 19 Nov 2024), and
907 sequences matching the $GABA_A$R/GlyR α-subunit domain (IPR006028) were retained.
908 No matches to the GlyR β-subunit domain (IPR008060) were detected. The final
909 alignment was trimmed with TrimAl[71] (v1.4.rev22) using the -gappyout flag.
910
911 A maximum-likelihood phylogeny was constructed using the IQ-TREE 2 server[72]
912 (v1.6.12; http://iqtree.cibiv.univie.ac.at/, accessed March 2025) under the LG+I+G4
913 substitution model selected by ModelFinder[73]. Branch support values were estimated
914 from 1,000 replicates using ultrafast bootstrap (-bb)[74] and SH-like approximate
915 likelihood-ratio tests (-alrt)[75]. Representative nicotinic acetylcholine receptor (nAChR)
916 subunits were included as an outgroup to root the tree. The resulting phylogeny was
917 visualized in FigTree (v1.4.4; http://tree.bio.ed.ac.uk/software/figtree/) and formatted
918 using Inkscape (v1.3; www.inkscape.org) and Adobe Illustrator (v30.0).
919
920 **AlphaFold structure prediction**
921 The predicted structure of the *Nematostella vectensis* $GABA_A$R-like subunit
922 NvGABAAR1 was generated using the AlphaFold3 web server[76]
923 (https://alphafoldserver.com, accessed June 2025), using the longest annotated RefSeq
924 isoform (gene ID: LOC5505184; protein ID: XP_048587017.1) as input. Predictions

925 were run with default parameters, and the top-ranked structural model was used for
926 visualization and structural comparison.
927
928 For cross-species comparison, AlphaFold-predicted structures of *Homo sapiens* GABA
929 type A receptor subunits GABRR3 (UniProt A8MPY1), GABRA2 (UniProt P47869), and
930 GABRG1 (UniProt Q8N1C3) were obtained from the AlphaFold Protein Structure
931 Database in July 2025. All human structures correspond to AlphaFold models version
932 v4 (AF-*-F1-v4).
933
934 Structural visualization and pairwise alignment were performed in UCSF ChimeraX[77]
935 (v1.9). All models were colored by per-residue model confidence, measured as
936 predicted Local Distance Difference Test (pLDDT), and aligned using the MatchMaker
937 algorithm.
938
939 **Use of AI tools**
940 Large language models (ChatGPT, OpenAI) were used under author direction to assist
941 with code generation, debugging, and improving the clarity of written text. All scientific
942 analyses, code execution, and validation were performed by the authors.
943
944 **Data availability**
945 Single-cell RNA-seq and bulk RNA-seq datasets generated in this study have been
946 deposited in the Gene Expression Omnibus (GEO) under accession numbers
947 GSE316974 and GSE316975. All source data will be deposited in the Stowers Original
948 Data Repository (ODR) prior to publication. Additional supporting data are available
949 from the corresponding author upon request.
950
951 **Code availability**
952 Custom R scripts used for data analysis and figure generation are provided with this
953 submission and will be made publicly available upon publication.
954

References

1. Bullock, T. & Horridge, G. A. *Structure and Function in the Nervous Systems of Invertebrates.* (San Francisco, Freeman, 1965).
2. Grimmelikhuijzen, C. J. P. & Westfall, J. A. The nervous systems of Cnidarians. in *The Nervous Systems of Invertebrates: An Evolutionary and Comparative Approach: With a Coda written by T.H. Bullock* (eds Breidbach, O. & Kutsch, W.) 7–24 (Birkhäuser Basel, Basel, 1995). doi:10.1007/978-3-0348-9219-3_2.
3. Holland, L. Z. *et al.* Evolution of bilaterian central nervous systems: a single origin? *EvoDevo* **4**, 27 (2013).
4. Arendt, D., Tosches, M. A. & Marlow, H. From nerve net to nerve ring, nerve cord and brain — evolution of the nervous system. *Nat. Rev. Neurosci.* **17**, 61–72 (2016).
5. Galliot, B. Hydra, a fruitful model system for 270 years. *Int. J. Dev. Biol.* **56**, 411–423 (2012).
6. Keramidioti, A. *et al.* A new look at the architecture and dynamics of the Hydra nerve net. https://doi.org/10.7554/elife.87330.2 (2024) doi:10.7554/elife.87330.2.
7. Hertwig, O. & Hertwig, R. K. W. T. von R. K. W. T. von H. S. *Die Actinien : Anatomisch Und Histologisch, Mit Besanderer Berücksichtigung Des Nervenmuskelsystems*. vol. Hft.1 (G. Fischer, Jena, 1879).
8. Robson, E. A. The nerve-net of a swimming anemone, Stomphia coccinea. *J. Cell Sci.* **S3-104**, 535–549 (1963).
9. Kinnamon, J. C. & Westfall, J. A. Types of neurons and synaptic connections at hypostome-tentacle junctions in *Hydra*. *J. Morphol.* **173**, 119–128 (1982).
10. Weissbourd, B. *et al.* A genetically tractable jellyfish model for systems and evolutionary neuroscience. *Cell* **184**, 5854-5868.e20 (2021).
11. Giez, C. *et al.* Satiety controls behavior in Hydra through an interplay of pre-enteric and central nervous system-like neuron populations. *Cell Rep.* **43**, 114210 (2024).
12. Bielecki, J., Dam Nielsen, S. K., Nachman, G. & Garm, A. Associative learning in the box jellyfish Tripedalia cystophora. *Curr. Biol.* **33**, 4150-4159.e5 (2023).
13. Oren, M. *et al.* Profiling molecular and behavioral circadian rhythms in the non-symbiotic sea anemone Nematostella vectensis. *Sci. Rep.* **5**, 11418 (2015).

14. Botton-Amiot, G., Martinez, P. & Sprecher, S. G. Associative learning in the cnidarian *Nematostella vectensis*. *Proc. Natl. Acad. Sci.* **120**, e2220685120 (2023).
15. Layden, M. J., Rentzsch, F. & Röttinger, E. The rise of the starlet sea anemone *Nematostella vectensis* as a model system to investigate development and regeneration. *WIREs Dev. Biol.* **5**, 408–428 (2016).
16. Carvalho, J. E., Burtin, M., Detournay, O., Amiel, A. R. & Röttinger, E. Optimized husbandry and targeted gene-editing for the cnidarian *Nematostella vectensis*. *Development* **152**, (2025).
17. Putnam, N. H. *et al.* Sea Anemone Genome Reveals Ancestral Eumetazoan Gene Repertoire and Genomic Organization. *Science* **317**, 86–94 (2007).
18. Zimmermann, B. *et al.* Topological structures and syntenic conservation in sea anemone genomes. *Nat. Commun.* **14**, 8270 (2023).
19. Fletcher, C. *et al.* The genome sequence of the starlet sea anemone, Nematostella vectensis (Stephenson, 1935). *Wellcome Open Res.* **8**, 79 (2023).
20. Ikmi, A., McKinney, S. A., Delventhal, K. M. & Gibson, M. C. TALEN and CRISPR/Cas9-mediated genome editing in the early-branching metazoan Nematostella vectensis. *Nat. Commun.* **5**, (2014).
21. Renfer, E. & Technau, U. Meganuclease-assisted generation of stable transgenics in the sea anemone Nematostella vectensis. *Nat. Protoc.* **12**, 1844–1854 (2017).
22. He, S. *et al.* An axial Hox code controls tissue segmentation and body patterning in *Nematostella vectensis*. *Science* **361**, 1377–1380 (2018).
23. Magie, C. R., Pang, K. & Martindale, M. Q. Genomic inventory and expression of Sox and Fox genes in the cnidarian Nematostella vectensis. *Dev. Genes Evol.* **215**, 618–630 (2005).
24. Anctil, M. Chemical transmission in the sea anemone Nematostella vectensis: A genomic perspective. *Comp. Biochem. Physiol. Part D Genomics Proteomics* **4**, 268–289 (2009).
25. Nakanishi, N., Renfer, E., Technau, U. & Rentzsch, F. Nervous systems of the sea anemone *Nematostella vectensis* are generated by ectoderm and endoderm and shaped by distinct mechanisms. *Development* **139**, 347–357 (2012).

1015 26. Layden, M. J., Boekhout, M. & Martindale, M. Q. *Nematostella vectensis achaete-*
1016 *scute*homolog*NvashA*regulates embryonic ectodermal neurogenesis and represents
1017 an ancient component of the metazoan neural specification pathway. *Development*
1018 **139**, 1013–1022 (2012).
1019 27. Sinigaglia, C., Busengdal, H., Leclère, L., Technau, U. & Rentzsch, F. The Bilaterian
1020 Head Patterning Gene six3/6 Controls Aboral Domain Development in a Cnidarian.
1021 *PLoS Biol.* **11**, e1001488 (2013).
1022 28. Sebé-Pedrós, A. *et al.* Cnidarian Cell Type Diversity and Regulation Revealed by
1023 Whole-Organism Single-Cell RNA-Seq. *Cell* **173**, 1520-1534.e20 (2018).
1024 29. Tournière, O. *et al.* NvPOU4/Brain3 Functions as a Terminal Selector Gene in the
1025 Nervous System of the Cnidarian Nematostella vectensis. *Cell Rep.* **30**, 4473-
1026 4489.e5 (2020).
1027 30. Cole, A. G. *et al.* Updated single cell reference atlas for the starlet anemone
1028 Nematostella vectensis. *Front. Zool.* **21**, 8 (2024).
1029 31. Faltine-Gonzalez, D. Z. & Layden, M. J. Characterization of nAChRs in Nematostella
1030 vectensis supports neuronal and non-neuronal roles in the cnidarian–bilaterian
1031 common ancestor. *EvoDevo* **10**, 27 (2019).
1032 32. Thiel, D. *et al.* Large-scale deorphanization of Nematostella vectensis neuropeptide
1033 G protein-coupled receptors supports the independent expansion of bilaterian and
1034 cnidarian peptidergic systems. *eLife* **12**, RP90674 (2024).
1035 33. Knabl, P., Mörsdorf, D. & Genikhovich, G. A whole-body atlas of BMP signaling
1036 activity in an adult sea anemone. *BMC Biol.* **23**, 49 (2025).
1037 34. Marlow, H., Matus, D. Q. & Martindale, M. Q. Ectopic activation of the canonical wnt
1038 signaling pathway affects ectodermal patterning along the primary axis during larval
1039 development in the anthozoan Nematostella vectensis. *Dev. Biol.* **380**, 324–334
1040 (2013).
1041 35. Matus, D. Q., Magie, C. R., Pang, K., Martindale, M. Q. & Thomsen, G. H. The
1042 Hedgehog gene family of the cnidarian, Nematostella vectensis, and implications for
1043 understanding metazoan Hedgehog pathway evolution. *Dev. Biol.* **313**, 501–518
1044 (2008).

1045 36. Ikmi, A. *et al.* Feeding-dependent tentacle development in the sea anemone
1046 Nematostella vectensis. *Nat. Commun.* **11**, 4399 (2020).
1047 37. Ikmi, A. & Gibson, M. C. Identification and In Vivo Characterization of NvFP-7R, a
1048 Developmentally Regulated Red Fluorescent Protein of Nematostella vectensis.
1049 *PLoS ONE* **5**, e11807 (2010).
1050 38. Leyva-Díaz, E., Masoudi, N., Serrano-Saiz, E., Glenwinkel, L. & Hobert, O.
1051 Brn3/POU-IV-type POU homeobox genes—Paradigmatic regulators of neuronal
1052 identity across phylogeny. *WIREs Dev. Biol.* **9**, (2020).
1053 39. Simeone, A. *et al.* Orthopedia, a novel homeobox-containing gene expressed in the
1054 developing CNS of both mouse and drosophila. *Neuron* **13**, 83–101 (1994).
1055 40. Steinmetz, P. R. *et al.* Six3 demarcates the anterior-most developing brain region in
1056 bilaterian animals. *EvoDevo* **1**, (2010).
1057 41. Owens, D. F. & Kriegstein, A. R. Is there more to gaba than synaptic inhibition? *Nat.*
1058 *Rev. Neurosci.* **3**, 715–727 (2002).
1059 42. Sequeira, A., Shen, K., Gottlieb, A. & Limon, A. Human brain transcriptome analysis
1060 finds region- and subject-specific expression signatures of GABAAR subunits.
1061 *Commun. Biol.* **2**, 153 (2019).
1062 43. Ojha, A. *et al.* Functional analysis of ligand-gated chloride channels in a cnidarian
1063 sheds light on the evolution of inhibitory signalling. *bioRxiv* 2025.07.26.666939
1064 (2025) doi:10.1101/2025.07.26.666939.
1065 44. Oren, M., Brikner, I., Appelbaum, L. & Levy, O. Fast Neurotransmission Related
1066 Genes Are Expressed in Non Nervous Endoderm in the Sea Anemone Nematostella
1067 vectensis. *PLoS ONE* **9**, e93832 (2014).
1068 45. Levy, S. *et al.* Ectopic activation of GABAB receptors inhibits neurogenesis and
1069 metamorphosis in the cnidarian Nematostella vectensis. *Nat. Ecol. Evol.* **5**, 111–121
1070 (2020).
1071 46. Koizumi, O. *et al.* The nerve ring in cnidarians: its presence and structure in
1072 hydrozoan medusae. *Zoology* **118**, 79–88 (2015).
1073 47. Nielsen, S. K. D., Koch, T. L., Wiisbye, S. H., Grimmelikhuijzen, C. J. P. & Garm, A.
1074 Neuropeptide expression in the box jellyfish *Tripedalia cystophora* —New insights

1075 into the complexity of a “simple” nervous system. *J. Comp. Neurol.* **529**, 2865–2882
1076 (2021).
1077 48. Genikhovich, G. & Technau, U. Induction of Spawning in the Starlet Sea Anemone
1078 *Nematostella vectensis* , In Vitro Fertilization of Gametes, and Dejellying of Zygotes.
1079 *Cold Spring Harb. Protoc.* **2009**, pdb.prot5281 (2009).
1080 49. Stefanik, D. J., Friedman, L. E. & Finnerty, J. R. Collecting, rearing, spawning and
1081 inducing regeneration of the starlet sea anemone, Nematostella vectensis. *Nat.*
1082 *Protoc.* **8**, 916–923 (2013).
1083 50. Layden, M. J., Röttinger, E., Wolenski, F. S., Gilmore, T. D. & Martindale, M. Q.
1084 Microinjection of mRNA or morpholinos for reverse genetic analysis in the starlet sea
1085 anemone, Nematostella vectensis. *Nat. Protoc.* **8**, 924–934 (2013).
1086 51. Renfer, E., Amon-Hassenzahl, A., Steinmetz, P. R. H. & Technau, U. A muscle-
1087 specific transgenic reporter line of the sea anemone, *Nematostella vectensis*. *Proc.*
1088 *Natl. Acad. Sci.* **107**, 104–108 (2010).
1089 52. *Whole-Body Regeneration: Methods and Protocols*. vol. 2450 (Springer US, New
1090 York, NY, 2022).
1091 53. Moreno-Mateos, M. A. *et al.* CRISPRscan: designing highly efficient sgRNAs for
1092 CRISPR-Cas9 targeting in vivo. *Nat. Methods* **12**, 982–988 (2015).
1093 54. Connelly, J. P. & Pruett-Miller, S. M. CRIS.py: A Versatile and High-throughput
1094 Analysis Program for CRISPR-based Genome Editing. *Sci. Rep.* **9**, 4194 (2019).
1095 55. Bates, D., Mächler, M., Bolker, B. & Walker, S. Fitting Linear Mixed-Effects Models
1096 Using **lme4**. *J. Stat. Softw.* **67**, (2015).
1097 56. Kuznetsova, A., Brockhoff, P. B. & Christensen, R. H. B. **lmerTest** Package: Tests in
1098 Linear Mixed Effects Models. *J. Stat. Softw.* **82**, (2017).
1099 57. Lenth, R. V. & Piaskowski, J. emmeans: Estimated Marginal Means, aka Least-
1100 Squares Means. (2025).
1101 58. Genikhovich, G. & Technau, U. Anti-acetylated Tubulin Antibody Staining and
1102 Phalloidin Staining in the Starlet Sea Anemone *Nematostella vectensis*. *Cold Spring*
1103 *Harb. Protoc.* **2009**, pdb.prot5283 (2009).

1104 59. Steinmetz, P. R. H., Aman, A., Kraus, J. E. M. & Technau, U. Gut-like ectodermal
1105 tissue in a sea anemone challenges germ layer homology. *Nat. Ecol. Evol.* **1**, 1535–
1106 1542 (2017).
1107 60. Goldfarb, T. *et al.* NCBI RefSeq: reference sequence standards through 25 years of
1108 curation and annotation. *Nucleic Acids Res.* **53**, D243–D257 (2025).
1109 61. Hao, Y. *et al.* Dictionary learning for integrative, multimodal and scalable single-cell
1110 analysis. *Nat. Biotechnol.* **42**, 293–304 (2024).
1111 62. Hafemeister, C. & Satija, R. Normalization and variance stabilization of single-cell
1112 RNA-seq data using regularized negative binomial regression. *Genome Biol.* **20**,
1113 296 (2019).
1114 63. Dobin, A. *et al.* STAR: ultrafast universal RNA-seq aligner. *Bioinformatics* **29**, 15–21
1115 (2013).
1116 64. Robinson, M. D., McCarthy, D. J. & Smyth, G. K. edgeR : a Bioconductor package
1117 for differential expression analysis of digital gene expression data. *Bioinformatics* **26**,
1118 139–140 (2010).
1119 65. Altschul, S. F., Gish, W., Miller, W., Myers, E. W. & Lipman, D. J. Basic local
1120 alignment search tool. *J. Mol. Biol.* **215**, 403–410 (1990).
1121 66. Blum, M. *et al.* InterPro: the protein sequence classification resource in 2025.
1122 *Nucleic Acids Res.* **53**, D444–D456 (2025).
1123 67. The UniProt Consortium *et al.* UniProt: the Universal Protein Knowledgebase in
1124 2025. *Nucleic Acids Res.* **53**, D609–D617 (2025).
1125 68. Li, W. & Godzik, A. Cd-hit: a fast program for clustering and comparing large sets of
1126 protein or nucleotide sequences. *Bioinformatics* **22**, 1658–1659 (2006).
1127 69. Fu, L., Niu, B., Zhu, Z., Wu, S. & Li, W. CD-HIT: accelerated for clustering the next-
1128 generation sequencing data. *Bioinformatics* **28**, 3150–3152 (2012).
1129 70. Katoh, K. & Standley, D. M. MAFFT Multiple Sequence Alignment Software Version
1130 7: Improvements in Performance and Usability. *Mol. Biol. Evol.* **30**, 772–780 (2013).
1131 71. Capella-Gutiérrez, S., Silla-Martínez, J. M. & Gabaldón, T. trimAl: a tool for
1132 automated alignment trimming in large-scale phylogenetic analyses. *Bioinformatics*
1133 **25**, 1972–1973 (2009).

72. Minh, B. Q. *et al.* IQ-TREE 2: New Models and Efficient Methods for Phylogenetic Inference in the Genomic Era. *Mol. Biol. Evol.* **37**, 1530–1534 (2020).
73. Kalyaanamoorthy, S., Minh, B. Q., Wong, T. K. F., Von Haeseler, A. & Jermiin, L. S. ModelFinder: fast model selection for accurate phylogenetic estimates. *Nat. Methods* **14**, 587–589 (2017).
74. Hoang, D. T., Chernomor, O., Von Haeseler, A., Minh, B. Q. & Vinh, L. S. UFBoot2: Improving the Ultrafast Bootstrap Approximation. *Mol. Biol. Evol.* **35**, 518–522 (2018).
75. Anisimova, M., Gil, M., Dufayard, J.-F., Dessimoz, C. & Gascuel, O. Survey of Branch Support Methods Demonstrates Accuracy, Power, and Robustness of Fast Likelihood-based Approximation Schemes. *Syst. Biol.* **60**, 685–699 (2011).
76. Abramson, J. *et al.* Accurate structure prediction of biomolecular interactions with AlphaFold 3. *Nature* **630**, 493–500 (2024).
77. Meng, E. C. *et al.* UCSF ChimeraX : Tools for structure building and analysis. *Protein Sci.* **32**, e4792 (2023).

Acknowledgements

We thank Boris Rubinstein and Kausik Si for discussions on behavioral experiments, and Kausik Si additionally for advice on neurotransmitter receptor composition analysis. We thank Joshua Zimmerberg for discussions on body size and nerve net scalability, and Neşet Özel for insights into the relevance of the vesicular GABA transporter in shaping interneuron identity. We are grateful to Mark Miller for creating the *Nematostella* life-cycle illustration, and to past and present members of the Gibson lab for discussions and support. We acknowledge the Stowers Technology Centers for assistance: the Aquatics team for animal husbandry; the Cytometry team, particularly Jillian Blanck, for cell sorting; the Sequencing and Discovery Genomics team for library preparation and sequencing; the Computational Biology team for processing of sequencing data; the Genome Engineering team for CRISPR genotyping; and the Microscopy Center for imaging training and support. This work was supported by the Stowers Institute for Medical Research.

Author contributions

R.Z. conceived and designed the study; performed all experiments and data analyses; prepared the figures; and wrote the manuscript. M.C.G. supervised the research, provided guidance, and edited the manuscript. C.W.S. performed preprocessing of sequencing data, generated genome-assembly mapping tables, and supervised code implementation. A.M.L.K. performed sequence alignment and phylogenetic tree construction. All authors reviewed and approved the final manuscript.

Competing interests

The authors declare no competing interests.

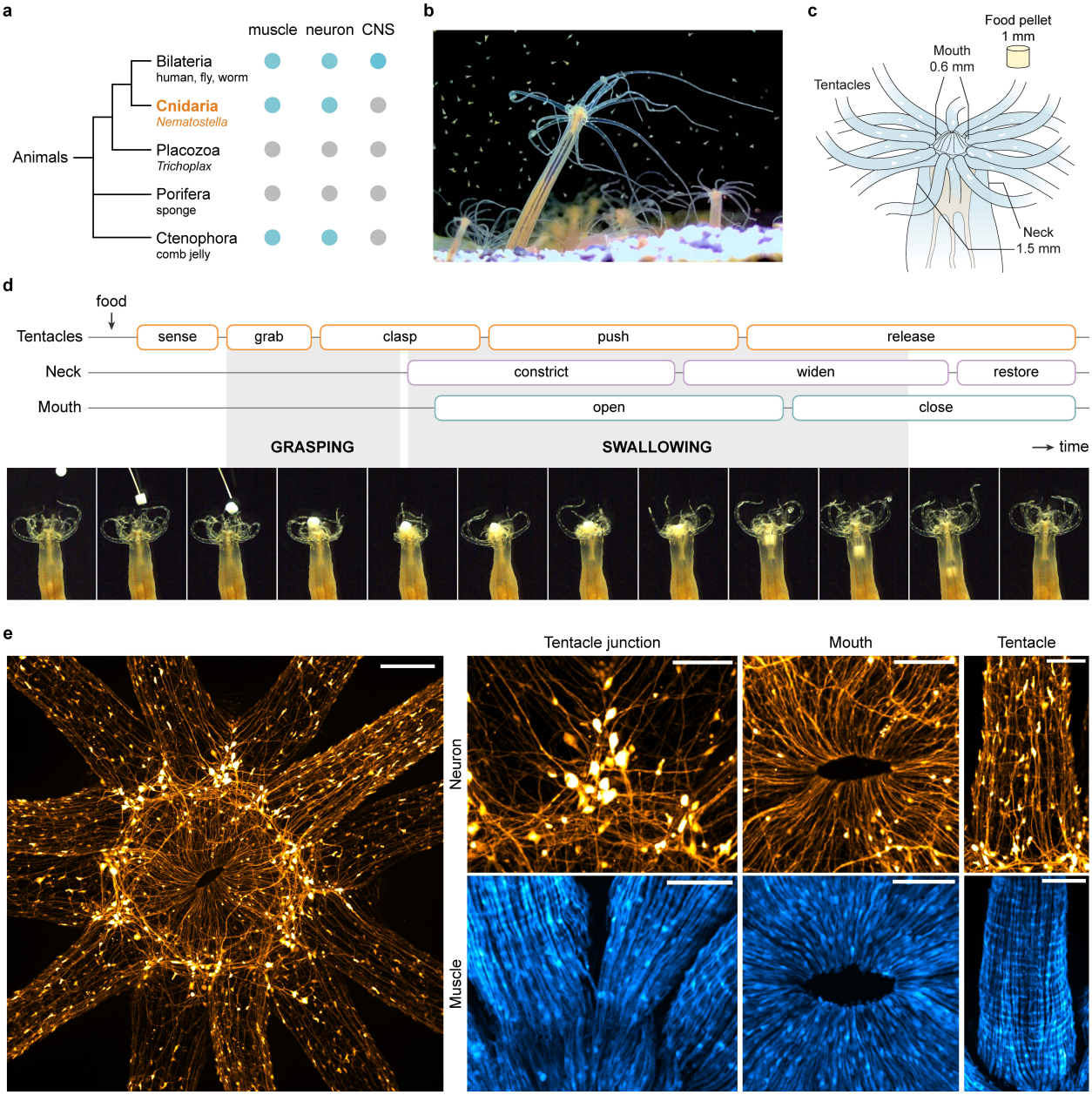

Fig. 1 | Structured motor coordination and a ganglion-like oral nerve ring in *Nematostella vectensis*.

(a) Phylogenetic distribution of muscles, neurons, and centralized nervous systems (CNS) across major animal lineages; the dotted branch indicates unresolved phylogenetic relationships. **(b)** Adult *Nematostella vectensis* partially buried in gravel while capturing live brine shrimp (*Artemia*). A corresponding video is provided in Supplementary Video 1. **(c)** Schematic of the standardized feeding paradigm, showing the relative geometry of the oral disc, tentacles, and neck, and the size of the food pellet

1185 (1 mm). **(d)** Time-lapse montage illustrating two sequential phases of feeding, grasping
1186 and swallowing, separated by the onset of neck constriction. Each phase is composed
1187 of coordinated motor subroutines executed by the tentacles, neck, and mouth. A
1188 corresponding time-lapse video is provided in Supplementary Video 6. **(e)** Live confocal
1189 images of juvenile *Nematostella vectensis* expressing the neuronal reporter
1190 *NvSH3GL3*^{P}*>mScarlet-I* (orange) or a muscle reporter driven by the myosin heavy chain
1191 promoter[51] (blue). Neuronal and muscle images were acquired from separate animals
1192 and are shown for anatomical reference. Left, overview of the oral region showing
1193 dense neuronal labeling in the oral disc and tentacles. Right, enlarged views of selected
1194 regions reveal distinct neuronal morphologies and spatial organization. Neurons with
1195 enlarged somata relative to surrounding neurons cluster at tentacle junctions and
1196 extend circumferential neurites, forming a ring-like pattern. Additional neurons exhibit
1197 smaller somata and distinct projection orientations, with radial projections around the
1198 oral opening and longitudinal projections within tentacles. Scale bars, 100 μm
1199 (overview) and 50 μm (enlarged views).
1200

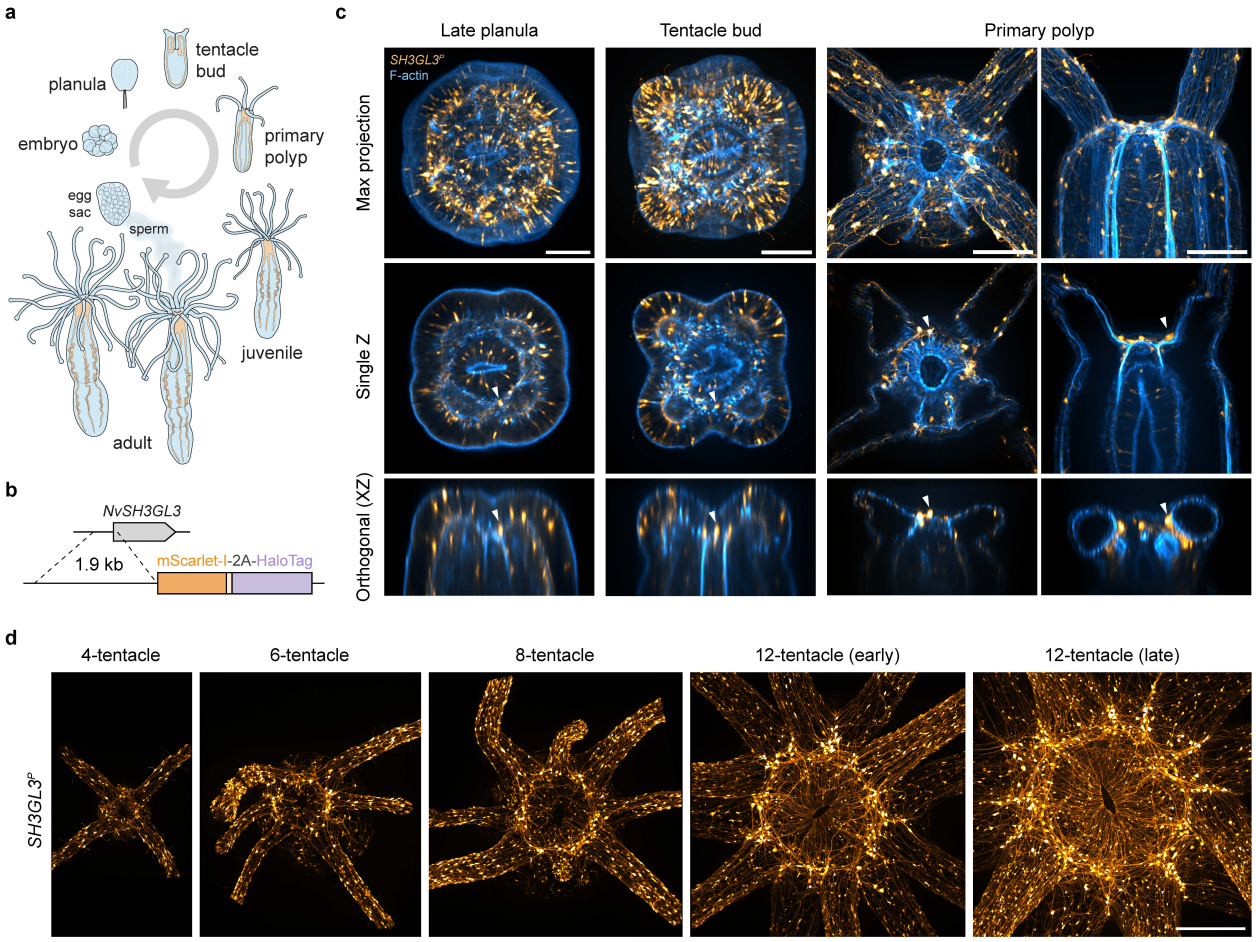

Fig. 2 | Developmental emergence and scaling of the oral nerve ring. **(a)** Schematic overview of *Nematostella vectensis* life stages, from embryo to adult, indicating the progressive addition of tentacles and the transition from planula larva to primary polyp and juvenile stages. **(b)** Schematic of the *NvSH3GL3*^{P} reporter construct. A 1.9 kb upstream regulatory region of *NvSH3GL3* drives expression of an mScarlet-I fluorescent reporter used to visualize neuronal morphology. **(c)** Confocal images showing *NvSH3GL3*^{P}*>mScarlet-I*–labeled neurons (orange) across early developmental stages, with F-actin staining (blue). Columns show late planula (3.5 days post-fertilization, dpf), tentacle buds (4.5 dpf), and primary polyps (10 dpf). Rows show maximum intensity projections (top), single optical sections (middle), and orthogonal (XZ) views (bottom). Late planula and tentacle-bud stages are shown in oral view, whereas primary polyps are shown in both oral and lateral views. In late planulae, sparsely distributed neurons with enlarged somata are observed in basal positions within the oral ectoderm. As tentacles emerge during the tentacle-bud and primary

1216 polyp stages, the number of these large-soma neurons increases, accompanied by
1217 higher neurite density and localization to the ectoderm at tentacle junctions. White
1218 arrowheads indicate representative neuronal somata shown in corresponding single
1219 optical sections and orthogonal views. Scale bars, 50 μm. **(d)** Oral-view maximum
1220 intensity projections showing *NvSH3GL3*^{P}*>mScarlet-I*–labeled neurons (orange) in
1221 polyps with increasing tentacle number (4, 6, 8, and 12). As polyps grow and
1222 sequentially add tentacles, the circumorally projecting neurite bundle that constitutes the
1223 oral nerve ring (ONR) becomes progressively denser, accompanied by increased
1224 accumulation of large neuronal somata at tentacle junctions. All panels are shown at the
1225 same scale. Scale bar, 200 μm.
1226

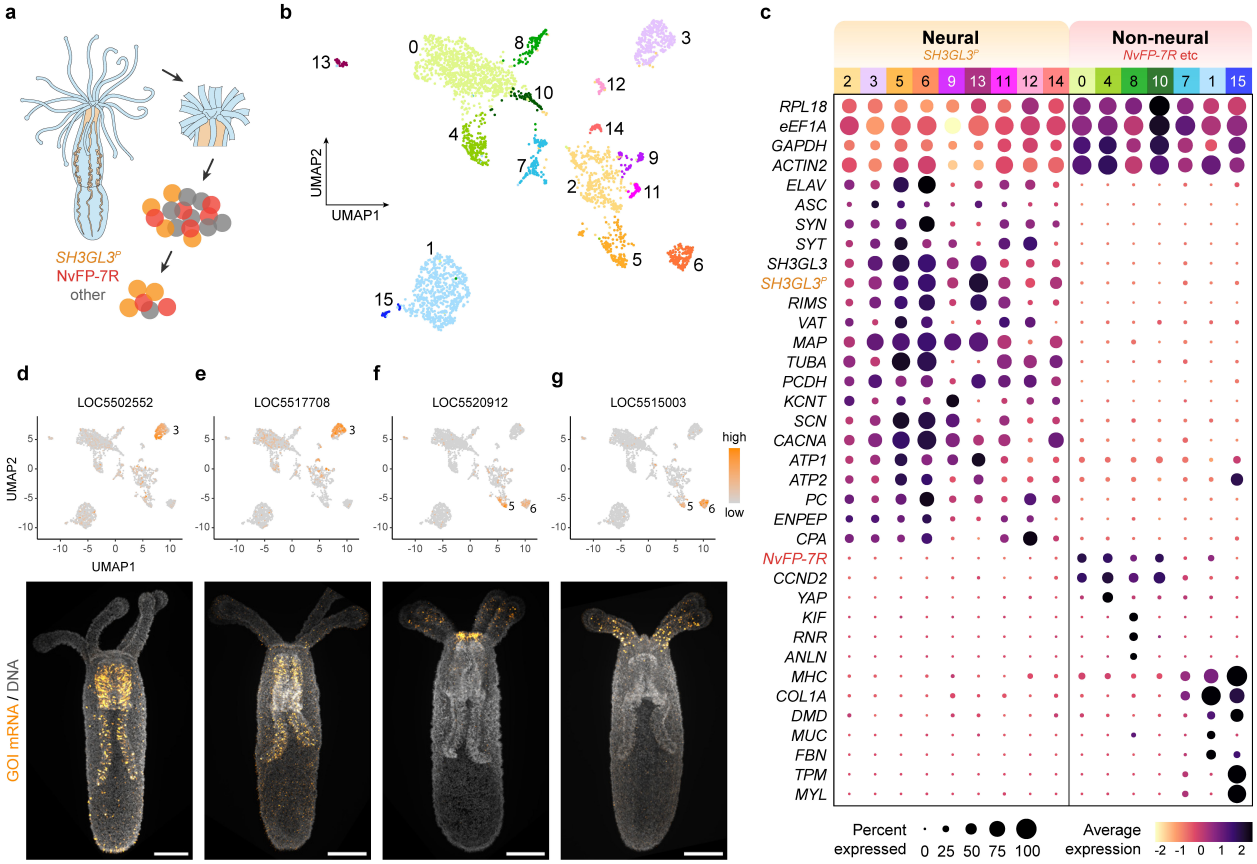

Fig. 3 | Molecular diversity and spatial organization of the oral nerve net. **(a)** Schematic of oral-end dissection and cell enrichment for single-cell RNA sequencing. Oral ends from adult *Nematostella vectensis* were dissected, and most tentacles were trimmed prior to mechanical and enzymatic dissociation for 10x Genomics single-cell RNA sequencing. Cells were enriched for *NvSH3GL3^{P}>mScarlet-I*-positive populations by fluorescence-activated cell sorting (FACS), with gating applied to reduce spectral contamination from cells expressing the native red fluorescent protein NvFP-7R. Colors indicate major cell populations (orange, *NvSH3GL3^{P}>mScarlet-I*; red, NvFP-7R; gray, other). **(b)** UMAP visualization of 3,297 cells from the single-cell dataset. **(c)** Dot plot showing representative gene categories, including housekeeping genes, canonical neuronal and synaptic markers, cytoskeletal components, ion channels and transporters, and adhesion/signaling molecules. Dot size indicates the percentage of cells expressing each gene, and color represents scaled average expression (pale yellow to dark purple). Neural clusters (left) show strong *SH3GL3^{P}* expression, whereas non-neural clusters (right) include *NvFP-7R*-enriched populations

1243 as well as clusters enriched for contractile, cytoskeletal, and extracellular-matrix genes.
1244 Expression of the *SH3GL3*^{P} reporter parallels endogenous *SH3GL3*, supporting reporter
1245 fidelity. A complete list of neural genes with identifiers is provided in Supplementary Fig.
1246 1a. **(d–g)** Feature plots (top) show SCT-normalized gene expression projected onto the
1247 UMAP, with corresponding fluorescent in situ hybridization (FISH) images (bottom) in
1248 four-tentacle primary polyps (7–10 dpf) for four representative cluster-enriched genes.
1249 (d,e) LOC5502552 and LOC5517708 are enriched in cluster 3 and display predominant
1250 expression in the pharyngeal region by FISH. (f,g) LOC5520912 and LOC5515003 are
1251 expressed in partially overlapping subsets of clusters 5 and 6 and show predominant
1252 FISH signal in the oral disc and tentacles. Feature plots are scaled independently for
1253 each gene, with light gray indicating no detectable expression and increasing color
1254 intensity indicating higher expression. DNA is shown in gray, and gene-specific signal is
1255 shown in orange. Scale bars, 100 μm.
1256

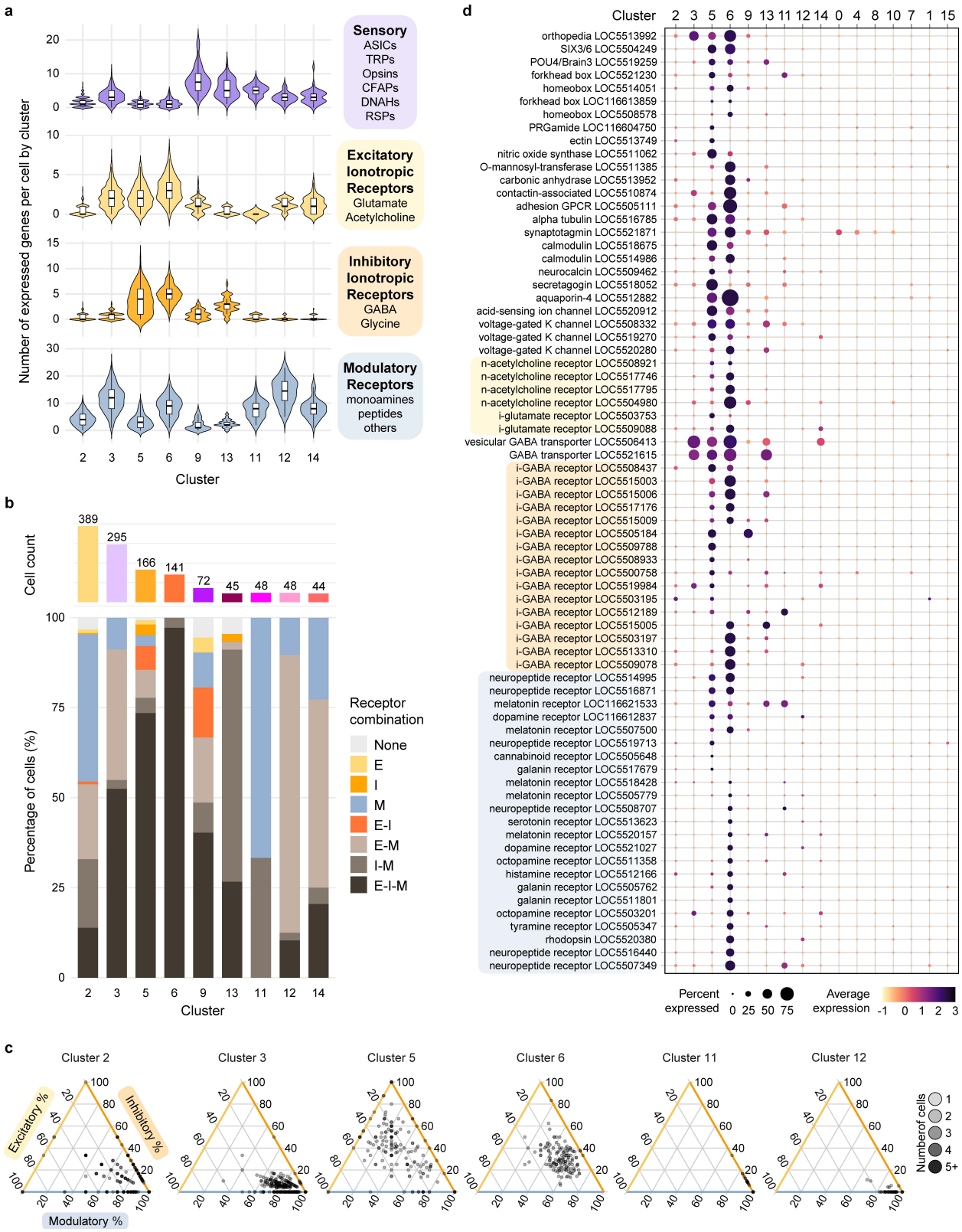

Fig. 4 | Integrative receptor repertoires distinguish interneuron-like neural clusters.

(a) Violin plots showing the number of sensory-related and neurotransmitter receptor genes detected per cell across neural clusters. Gene categories are color-coded as sensory (purple), ionotropic excitatory (E, gold), ionotropic inhibitory (I, orange), and metabotropic/modulatory (M, blue). **(b)** Co-expression analysis of E/I/M receptor combinations across neural clusters. The upper histogram shows total cell counts per cluster, and the lower stacked bar plot shows the percentage of cells in each cluster belonging to different receptor-class combination categories. Pale gray denotes cells lacking detectable neurotransmitter receptors; gold, excitatory-only; orange, inhibitory-only; blue, modulatory-only; orange-red, excitatory–inhibitory; light gray, excitatory–modulatory; medium gray, inhibitory–modulatory; and dark gray, cells co-expressing all three receptor classes. **(c)** Ternary plots showing the relative proportions of detected E, I, and M receptors per cell for selected clusters. Each point represents a cell, positioned according to its E/I/M receptor composition. Point color indicates the number of overlapping cells sharing the same receptor ratio, from light gray (1 cell) to black (≥ 5 cells). **(d)** Dot plot showing expression patterns of transcription factors, synaptic components, ion channels, and neurotransmitter receptors associated with fast neurotransmission and neuromodulation across clusters. Dot size indicates the percentage of cells expressing each gene, and color represents scaled average expression (pale yellow to dark purple). Gold, orange, and blue shading highlight genes belonging to the E, I, and M receptor families, respectively.

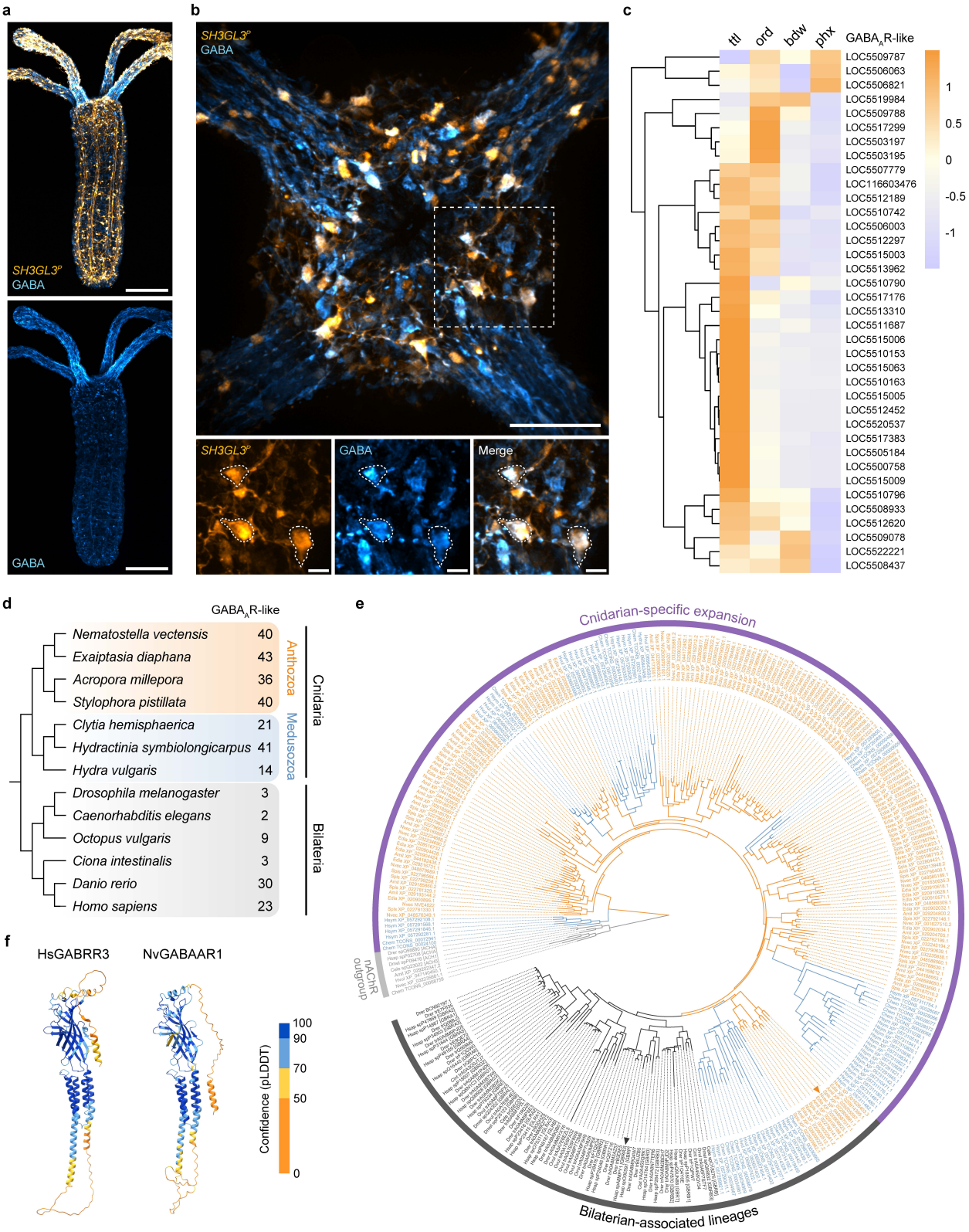

Fig. 5 | Expansion and oral enrichment of ionotropic GABAergic signaling components.

1284 **(a)** Whole-mount γ-aminobutyric acid (GABA) immunostaining of
1285 *NvSH3GL3^{P}>mScarlet-I* primary polyps, showing enriched GABA immunoreactivity in
1286 the oral disc and tentacles. Scale bars, 100 µm. **(b)** Within the oral disc, GABA
1287 immunoreactivity is restricted to large-soma cells, including both mScarlet-I-positive
1288 neurons and additional large-soma GABA-positive cells lacking reporter signal. Top,
1289 merged image of *SH3GL3^{P}* (orange) and GABA (blue), with the dashed box indicating
1290 the region shown below. Bottom, split-channel views of the boxed region (*SH3GL3^{P}*,
1291 left; GABA, middle; merge, right). Dashed outlines mark representative large-soma cells
1292 that are double-positive for *SH3GL3^{P}* and GABA. GABA accumulation is also visible in
1293 varicosities along neurites. Scale bars, 50 µm (top), 10 µm (bottom). **(c)** Heatmap
1294 showing tissue-specific expression of GABA type A receptor-like ($GABA_AR$-like)
1295 homologs in adult *Nematostella*. Colors indicate Z-scored average TPM per gene
1296 across tissues (ttl, tentacles; ord, oral disc; bdw, oral body wall; phx, pharynx), with
1297 warmer colors representing higher relative expression. **(d)** Gene counts of $GABA_AR$-like
1298 homologs across seven cnidarian species (four anthozoans, three medusozoans) and
1299 six bilaterian species. Anthozoans (orange) and medusozoans (blue) show marked
1300 expansion of the receptor family relative to bilaterians (dark gray). **(e)** Maximum-
1301 likelihood phylogeny of $GABA_AR$-like homologs based on amino-acid sequences from
1302 the species set in (d). Anthozoan sequences are shown in orange, medusozoan
1303 sequences in blue, and bilaterian sequences in dark gray; representative nicotinic
1304 acetylcholine receptor (nAChR) subunits (light gray) form an outgroup to root the tree.
1305 Outer arcs denote the cnidarian-specific expansion (orange) and the bilaterian-
1306 associated lineage (dark gray). Arrowheads indicate the *Nematostella* subunit
1307 NvGABAAR1 (orange) and the human subunit GABRR3 (dark gray) selected for
1308 structural comparison in (f). Branch support for the cnidarian–bilaterian split was
1309 assessed with ultrafast bootstrap and SH-like aLRT values of 92.3 and 80; full support
1310 values are shown in Supplementary Fig. 4. **(f)** AlphaFold-predicted structures of *Homo*
1311 *sapiens* GABRR3 (γ-aminobutyric acid type A receptor subunit ρ3) and its *Nematostella*
1312 *vectensis* homolog NvGABAAR1 (protein ID: XP_048587017.1; gene ID: LOC5505184),
1313 corresponding to the subunits marked by arrowheads in (e). Ribbon coloring indicates

1314 per-residue model confidence (pLDDT): orange (0–50), yellow (50–70), light blue (70–
1315 90), and dark blue (90–100).
1316

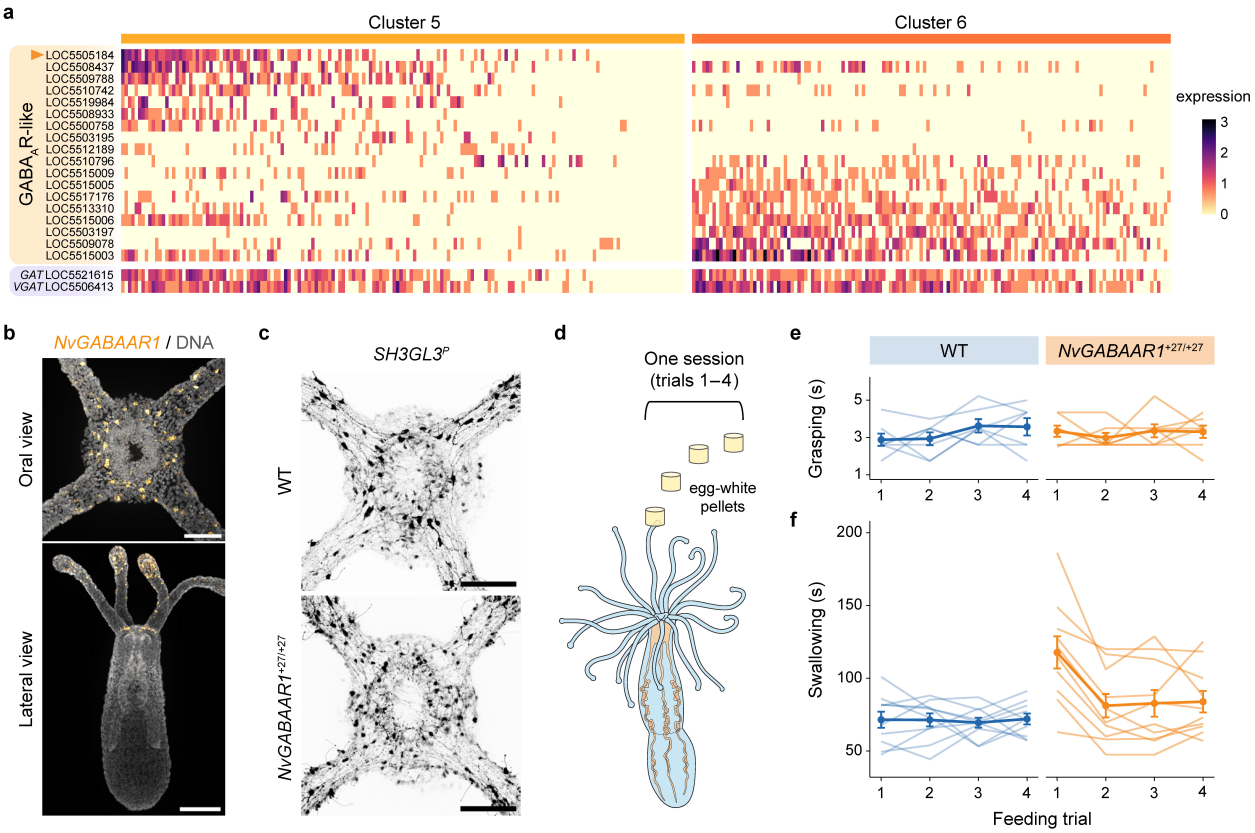

Fig. 6 | Loss of *NvGABAAR1* selectively delays swallowing initiation during feeding.

(a) Heatmap showing SCT-normalized expression of genes involved in GABA signaling across single cells from clusters 5 and 6. The gene set includes multiple GABA$_A$R-like subunits as well as the plasma membrane GABA transporter (*GAT*) and vesicular GABA transporter (*VGAT*). Columns represent individual cells ordered within each cluster by aggregate expression of this gene set. Rows are grouped by gene category and arranged from cluster 5-enriched (top) to cluster 6-enriched (bottom). The orange arrowhead marks LOC5505184 (*NvGABAAR1*), the subunit highlighted in Fig. 5e and analyzed functionally in Fig. 6b–f. **(b)** FISH in four-tentacle primary polyps showing *NvGABAAR1* expression restricted to the oral region, including the oral disc and a subset of tentacle neurons. *NvGABAAR1* signal in orange; DNA counterstain in gray. Top, oral view; bottom, lateral view. Scale bars, 50 µm (top), 100 µm (bottom). **(c)** Confocal images of wild-type (WT) and *NvGABAAR1*$^{+27/+27}$ primary polyps in the *NvSH3GL3*^{P}*>mScarlet-I* reporter background. The organization of the oral nerve ring appears comparable at the level of gross morphology between WT and mutants. Scale

bars, 50 μm. **(d)** Feeding assay design. Each behavioral session consisted of four sequential presentations of 1 mm × 1 mm egg-white pellets delivered to the oral disc. **(e)** Grasping duration across four feeding trials using pipette-delivered food pellets. Thin lines represent individual animals (WT in blue, n = 7; *NvGABAAR1*$^{+27/+27}$ mutants in orange, n = 7); bold lines and error bars denote mean ± s.e.m. Grasping duration was comparable between genotypes. **(f)** Swallowing duration across four feeding trials. Animals were assayed using either pipette or whisker delivery (each animal was tested with a single method throughout its session). Delivery method did not affect the genotype × trial interaction (see Methods), so data were analyzed together. Thin lines represent individual animals (WT in blue, n = 10; mutants in orange, n = 10); bold lines and error bars denote mean ± s.e.m. Mutants exhibited a pronounced increase in swallowing duration on trial 1 (46.6 ± 10.1 s; p = 0.0001) but converged to WT-like performance on trials 2–4. Full statistical details are provided in Supplementary Table 8.